POD-based analysis of a wind turbine wake under the influence of tower and nacelle

Giovanni de Cillis, Stefania Cherubini, Onofrio Semeraro, Stefano Leonardi, Pietro de Palma

Received: 14 January 2020 | Revised: 11 September 2020 | Accepted: 29 October 2020
DOI: 10.1002/we.2592

RESEARCH ARTICLE

WILEY

POD-based analysis of a wind turbine wake under the influence of tower and nacelle

Giovanni De Cillis[1,2] | Stefania Cherubini[1] | Onofrio Semeraro[3] | Stefano Leonardi[2] | Pietro De Palma[1]

[1]Department of Mechanics, Mathematics and Management, Polytechnic University of Bari, Bari, Italy

[2]Department of Mechanical Engineering, University of Texas at Dallas, Richardson, Texas, USA

[3]LIMSI, CNRS, Paris-Saclay University, Orsay, France

Correspondence
Giovanni De Cillis, Department of Mechanics, Mathematics and Management, Polytechnic University of Bari, Via Re David 200, 70125 Bari, Italy.
Email: giovanni.decillis@poliba.it

Abstract

The wake produced by a model wind turbine is investigated using proper orthogonal decomposition (POD) of numerical data obtained by large eddy simulations at a diameter-based Reynolds number $Re = 6.3 \times 10^5$. The blades are modeled employing the actuator line method and an immersed boundary method is used to simulate tower and nacelle. Two simulations are performed: one accounts only for the blades effect; the other includes also tower and nacelle. The two simulations are analyzed and compared in terms of mean flow fields and POD modes that mainly characterize the wake dynamics. In the rotor-only case, the most energetic modes in the near wake are composed of high-frequency tip and root vortices, whereas in the far wake, low-frequency modes accounting for mutual inductance instability of tip vortices are found. When tower and nacelle are included, low-frequency POD modes are present already in the near wake, linked to the von Karman vortices shed by the tower. These modes interact nonlinearly with the tip vortices in the far wake, generating new low-frequency POD modes, some of them lying in the frequency range of wake meandering. An analysis of the mean kinetic energy (MKE) entrainment of each POD mode shows that tip vortices sustain the wake mean shear, whereas low-frequency modes contribute to wake recovery. This explains why tower and nacelle induce a faster wake recovery.

KEYWORDS

entrainment, LES, POD, tip vortices, wake recovery

1 | INTRODUCTION

In order to limit the negative impact of energy production by fossil fuels on the environment and climate equilibrium, in the upcoming years, a larger fraction of energy demand must be satisfied by renewable sources. In 2018, 80% of the global energy consumption has been provided by fossil fuels (coal, oil, and gas).[1] The energy production from renewable sources increased by 4% in 2018,[1] accounting for almost one quarter of global energy demand growth. Onshore wind energy production is expected to expand by 12.5% between 2019 and 2024.[2]

Achieving such a target requires the design and installation of new large wind farms, constituted of up to hundreds of turbines, and the upgrade of existing ones exploiting new technologies for improving efficiency and reliability. When clustered in large farms, a great part of the wind turbines operates in the wake of upwind turbines. The velocity deficit and the high turbulence level of the incoming flow induces power losses and fatigue blade loading.[3-5] For this reason, understanding the dynamics of wind turbine wakes is fundamental for the design and optimization of wind turbines and farms. However, this is a challenging task due to the multiscale nature of atmospheric turbulence spreading over a wide range of spatial scales ranging from millimeters, corresponding to the Kolmogorov turbulence length scale, influencing the flow past the blade airfoils, to thousands of kilometers, linked to the horizontal length scale of the vortices in the atmosphere, influencing the interaction between the ABL and large wind farms.[6] Notably, the entrainment of energy from the flow above the wind turbines appears to be dominated by large-scale structures having at least the size of the rotor diameter.[7]

Wind turbine wakes, similarly to many other turbulent flows, are characterized by coherent motions with characteristic wavelengths and lifetimes, presenting a strong correlation over both space and time, the so-called coherent structures.[8,9]

One of the most widely used methods for extracting coherent structures from flow data is the proper orthogonal decomposition (POD).[10-12] POD allows one to find a finite set of deterministic modes whose linear combination optimally reconstructs the energy of a set of stochastic flow data. Such a technique has been recently introduced in the study of the flow through wind turbines and wind farms. Andersen et al.[13] simulated the turbulence in the interior of a wind farm using large eddy simulation and the actuator line method. The flow was reconstructed by applying the POD to the velocity field extracted in a plane perpendicular to the streamwise direction. VerHulst and Meneveau[14] proposed one of the first applications of the three-dimensional POD analysis to the study of a wind farm. They classified the resulting POD modes into four categories according to their general structure and determined how many of these POD modes are needed to capture a large fraction of the turbulent kinetic energy of the flow.

Sarmast et al.[15] focused on the stability properties of the tip vortices and the mechanisms leading to vortex pairing by means of large eddy simulation (LES), continuing the work previously performed by Ivanell et al.[16] The flow was perturbed by using low-amplitude excitations near the tip of the blades and the POD technique was employed to extract the unstable modes demonstrating a prominence of the mutual inductance phenomenon.

Also, Bastine et al.[17] applied the two-dimensional POD to the LES data of the wake of a wind turbine, considering a more realistic incoming flow representing a turbulent atmospheric boundary layer (ABL) in the case of a neutrally stratified atmosphere. Hamilton et al.[18,19] investigated wake interaction and recovery dynamics in different wind turbine array configurations using the POD applied to velocity measurements. Resulting modes were used for constructing low-dimensional models of turbulence statistics. Double POD applied on a similar dataset[20] has indicated that the structure of the wake can be described using a small subset of the original mode basis, providing a total reduction to 0.015% of the degrees of freedom of the wind turbine wake. Very recently,[21] POD analysis applied to LES data with actuator disk model has been used to construct a reduced-order model of turbine wakes using polynomial reconstruction able to quantify the interaction and evolution of the POD modes. POD has been also used to extract coherent structures of the thermally stratified wind turbine array boundary layer,[22] showing that, in the unstable and neutrally stratified regimes, the structures related to the ABL flow, which are beneficial for wake recovery, dominate over those introduced by the presence of the turbines. The effect of the spacing between wind turbines on POD modes has been assessed by Ali et al.,[23] showing that modifying the streamwise and spanwise spacing leads to changes in the background structure of the turbulence as well as on power producted. Numerous other works focused on the wake of a single wind turbine. Sørensen et al.[24] applied the POD on the LES results for a single-turbine wake analyzing the flow field in planes behind the rotor. The spatial development of the POD modes was employed to describe the breakdown process in the transition region from the near wake to the far wake. Bastine et al.[25] applied the POD technique to LES data, extracted in one plane in the wake, to investigate a new stochastic modeling approach for the wake of a wind turbine. They showed that approximately six POD modes are sufficient to capture the load dynamics on large temporal scales. Debnath et al.[26] studied the dynamics of wind turbine wakes and instabilities of helicoidal tip vortices using three-dimensional POD. Snapshots of the velocity field obtained from the LES of an isolated wind turbine were considered as dataset. The dominant wake structures were selected for the formulation of a reduced-order model.

Despite providing a thorough analysis of the energy-containing coherent structures behind a rotor, most of these works neglect the contribution of tower and nacelle to the flow dynamics. However, their influence is fundamental for understanding the behavior of the wake and for correctly estimating its recovery and the main flow frequencies. The coherent motion in a wind turbine wake can be divided into two regions with different dynamics, the near-wake region and the far-wake region, characterized by radically different coherent structures. In the near wake, coherent helicoidal vortex structures are shed from the tip and the root of the rotor blades.[13] In general, the coherent tip and root vortex systems undergo instability mechanisms and break down forming small-scale turbulent structures. Mutual inductance between the spirals of the helicoidal vortices is one of the main instability mechanisms, leading to vortex pairing in the rotor wake.[16] At the center of the near wake, there is the so-called hub vortex, a vortical structure elongated in the streamwise direction[27,28] and characterized by a single-helix counter-winding periodic instability, which may interact with the tip vortices triggering the breakdown of the vortex system.[29,30] The central part of the near wake can be also characterized by a vortex shedding mechanism typical of bluff bodies due to the presence of the nacelle.[31] The far wake, in contrast, is less dependent on the geometry of the turbine and is characterized by turbulent structures derived from the breakdown of coherent vortices and by the entrainment of the outer flow leading to wake recovery.[32,33]

Although many studies have essentially focused on the vortical dynamics induced by the rotor, the tower and nacelle are now believed to have a fundamental role in the breakdown of the vortices shed by the rotor and on the consequent wake recovery. The wake of the tower appears to promote the breakdown of the tip vortices, increasing the MKE flux into the wake.[34] Similarly to background turbulence, tower–wake interactions also induce an asymmetry of the wake deficit, leading to a decreased efficiency and increased blade stress levels for a turbine placed downstream.[35] Moreover, the role of the nacelle on the origin of wake meandering in the near field of a single turbine has been recently investigated.[30] The helical hub vortex that forms behind the turbine nacelle interacts with the tip vortices while expanding radially, leading to turbulent coherent structures in the far wake that can be connected to the wake meandering phenomenon.[36] For this reason, incorporating the presence of the nacelle in wind farm simulations is crucial for accurately predicting the dynamics of wake meandering as well as the loads on downwind turbines.[37] Nevertheless, most of these studies including the effect of tower and nacelle focus on the features of the mean flow only, failing to capture unsteady phenomena due to the interaction of coherent structures with different frequencies and structures, which may have a strong impact on wake entrainment and recovery. An analysis of the influence of both tower and nacelle on the main frequencies and spatial features of the coherent structures developing in the turbine wake, which is at the moment still lacking, will be crucial to determine the impact of these components of a wind turbine on the entrainment and recovery of its wake.

The present work attempts to fill this gap, aiming at assessing the effect of tower and nacelle on the dynamics of coherent structures in the wake of wind turbines. To identify the most relevant coherent structures, the numerically simulated flow in the presence and absence of tower and nacelle has been analyzed using the POD technique. This work provides one of the rare applications of the POD technique to a full three-dimensional set of data for a wind turbine, comparing the wake generated by an isolated (ideal) turbine rotor with that generated by the complete turbine including the tower and nacelle. In the authors' knowledge, a similar analysis has been previously carried out only by Debnath et al.[26] with main focus on the construction of a reduced-order model based on POD modes rather than on the analysis of the physical meaning of the different modes. In this work, we are interested in a fine analysis of the coherent structures recovered by POD in the near and in the far wake, aiming at unraveling the physical mechanisms enhancing or hindering wake recovery. The outcomes of the POD analysis in the two different configurations (rotor-only and complete turbine) will be compared in order to understand the role of tower and nacelle in wake recovery and meandering. At this purpose, we have employed an LES approach to solve the Navier–Stokes equations.[38] The geometry of the tower and the nacelle is modeled by an immersed boundary method,[34,39] whereas the actuator line method[40,41] is used for modeling the rotor blades. For the present computations, a model turbine geometry has been considered, which has been tested in a wind tunnel and provides us a benchmark for our numerical results. The exact experimental conditions were reproduced with the same numerical code used here by Santoni et al.,[34] and the numerical results agreed well with measurements. In the present paper, we have slightly modified the geometrical setup to decrease the blockage of the flow. We have also reduced the radius of the tower and the length of the nacelle in order to have conditions closer to utility-scale turbines and increase the impact of our findings. The experiments were conducted at relatively low Reynolds number and with a very weak level of inlet turbulence intensity, so that we have neglected the inlet turbulence in the computations. Inlet turbulence may have an influence on the dynamics of the wake and also on the interaction of the tower and nacelle wakes with the tip and root vortex helices. However, the coherent structures generated in the wake of the tower and the nacelle have given length scales and range of frequency which are mainly dependent on the geometry of these two components and on the incoming flow velocity. Therefore, the present flow analysis provides an interesting insight in the mechanism of the diffusion of the wake, which is valid for low values of the inlet turbulence intensity and Reynolds number.

The present paper is organized as follows. Section 2 provides an overview of the numerical methods used in this work. Section 3 presents the numerical setup for the LESs. The computed mean flow is discussed in Section 4, whereas the POD analysis is presented in Section 5, at first in the rotor-only case (Section 5.1) and then in the presence of tower and nacelle (Section 5.2). In Section 5.3, the POD modes recovered in these two configurations are compared. An analysis of the contribution of each POD mode on the MKE entrainment is provided in Section 6. Finally, relevant conclusions are drawn in Section 7.

2 | METHODOLOGY

In this work, we use LES to study the wake behind a wind turbine. This type of computational approach solves in a direct way the large-scale turbulent structures, with shape and wavelength depending on the geometry of the problem, that contain a large part of the energy of the flow, whereas smaller-scale turbulent fluctuations, which do not depend on the geometry of the considered problem, are filtered out and their effect on the larger flow structures is modeled. Therefore, LES allows one to reduce the computational cost with respect to direct numerical simulation (DNS), achieving at the same time a much higher accuracy with respect to the Reynolds-averaged Navier–Stokes equations, especially for flows where large-scale motions are significant, such as flows over bluff bodies.[42] LESs are carried out by solving the governing equations for the filtered nondimensional velocity, $\boldsymbol{u}$, and pressure, p, derived from the Navier–Stokes equations for incompressible flows:

$$\frac{\partial u_i}{\partial t}+\frac{\partial u_i u_j}{\partial x_j}=-\frac{\partial p}{\partial x_i}+\frac{1}{Re}\frac{\partial^2 u_i}{\partial x_j \partial x_j}-\frac{\partial \tau_{ij}}{\partial x_j}+F_i, \tag{1}$$

$$\frac{\partial u_i}{\partial x_i} = 0, \tag{2}$$

where $i,j \in \{1,2,3\}$ indicate the components in the Cartesian reference frame corresponding to the streamwise, x, wall-normal, y, and spanwise, z, directions, respectively. The Reynolds number is defined as $Re = U_\infty D/\nu$, where U_∞ is the inlet velocity, D is the rotor diameter, and ν is the kinematic viscosity of the fluid, which have been used as reference variables (viz., $x = X/D, y = Y/D, z = Z/D$ and $u_i = U_i/U_\infty$). The subgrid-scale stress tensor, τ_{ij}, can be decomposed into an isotropic part and an anisotropic part, τ_{ij}^r. The isotropic part is included in the modified filtered pressure $p^* = p + \frac{1}{3}\tau_{ii}$, whereas the anisotropic part is modeled using the Smagorinsky model with constant $C_s = 0.09$. The Smagorinsky model has been widely used for similar test cases (see, for instance, the work of Martinez-Tossas et al.[41]). Ciri et al.[43,44] performed LES of the "Blind test 1"[45] and the "Blind test 4"[46] using the Smagorinsky model varying the value of C_S, the Vreman, the WALE, and the σ models. They indicated a weak dependence of the wake dynamics on the particular subgrid-scale model, similarly to the results of Sarlak et al.[47] Therefore, in the present paper, we employed the Smagorinsky model because it is already validated in these previous studies. The last term in Equation (1), F_i, represents the force per unit volume given by the actuator line method, which models the aerodynamic forces exerted by the turbine blades on the fluid, as further explained in Appendix A1. The tower and nacelle are described using the immersed boundary method (see Appendix A1 for details). The governing equations are solved using a second-order-accurate centered finite difference scheme on a staggered Cartesian grid and an hybrid low-storage third-order-accurate Runge–Kutta scheme for time integration.[48]

3 | SIMULATION LAYOUT

The simulation layout is based on the experiments performed by Krogstad and Eriksen[45] using a turbine model with a three-bladed rotor of diameter $D = 0.894\text{m}$ and hub height $y_h = 0.817\text{m}$. Detailed information about the blade design is given in Krogstad and Eriksen.[49] The tower is modeled as a cylinder with diameter equal to one-tenth of the rotor diameter, namely, $d_t = 8.94\text{cm}$. The nacelle is modeled as a capsule with the same diameter of the tower having an axial length of 0.298m (0.3D). The computational domain (Figure 1) has dimensions $12.5D \times 5D \times 3D$ in the streamwise (x), wall-normal (y) and spanwise (z) directions, respectively. The rotor is located at 4D from the inlet section and it is centered in the

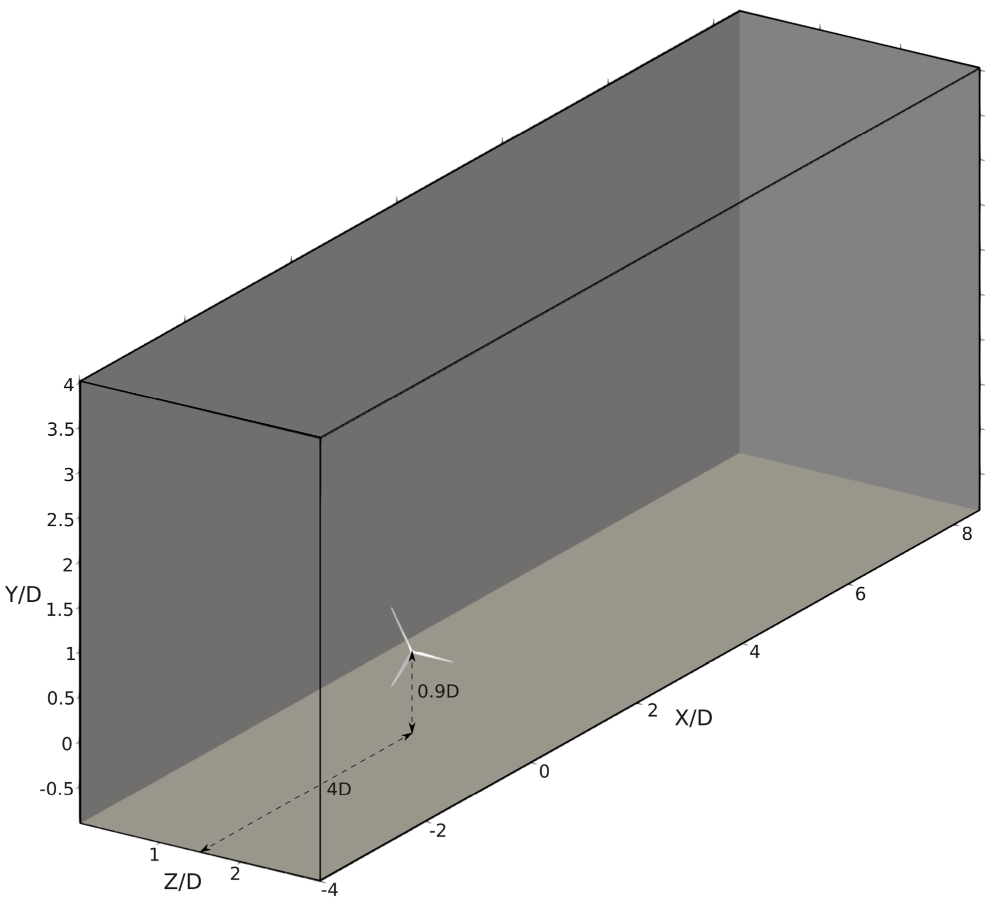

FIGURE 1 Computational domain [Colour figure can be viewed at wileyonlinelibrary.com]

spanwise direction. A uniform velocity profile aligned with the rotor axis with $U_\infty = 10\text{m}/\text{s}$ is imposed at the inlet points, whereas a radiative boundary condition is employed at the outlet points with uniform convection velocity $C = 9\text{m}/\text{s}$.[50] The no-slip condition is imposed at the bottom wall, whereas free slip is prescribed at the top wall. The lateral boundaries are periodic. Since the working fluid is air at atmospheric pressure and 10°C, the Reynolds number is $Re = 6.3 \times 10^5$. The computational domain is discretized using $2048 \times 512 \times 512$ grid points in x, y, and z directions, respectively. The grid point distribution is uniform along the streamwise and spanwise directions, whereas it is stretched in the wall-normal direction, with finer (uniform) spacing in the rotor wake region. Following the experimental data,[45] the tip speed ratio considered in this study is $\lambda = 3$, which implies a constant dimensionless angular frequency of the rotor:

$$\Omega = \frac{2\lambda U_{ref}}{U_\infty} = 6, \tag{3}$$

since we have chosen the inlet velocity U_∞ as reference velocity U_{ref}. The corresponding Strouhal number is $St_r = \Omega/2\pi = 0.9549$. It has to be pointed out that the chosen flow configuration does not reproduce exactly that of the reference case.[45] In particular, we have reduced the blockage effect by removing lateral walls and extending the domain in the wall-normal direction up to five diameters, and we have decreased the dimensions of tower and nacelle, in order to render the setup more similar to that of utility-scale wind turbines.

4 | MEAN FLOW FIELDS

4.1 | Time-averaged velocity fields

In the present section, the time-averaged flow fields computed for the two flow configurations, the first considering only the rotor and the second taking into account tower and nacelle, are discussed and compared. In the remainder of the paper, we will refer to the rotor-only case and the tower and nacelle flow configurations as the RO and the TN cases, respectively.

As shown in Figure 2, in the $x = 1$ plane, for both configurations, the wake is asymmetric in the vertical (y, z) plane, and the near-wake flow rotates in the direction opposed to that of the rotor. When the nacelle is neglected, an unphysical jet develops at the center of the rotor, whose strength increases with the tip speed ratio.[34] The presence of the tower and nacelle increases the asymmetry of the flow due to the presence of additional wakes behind the tower and at the center of the wake due to the nacelle. One can clearly observe in Figure 2B that the left part of the near-wake flow has a lower velocity than the right one. This is due to the transport of low-momentum fluid from the wake of the tower, which is lifted up in the near-wake region. Finally, two asymmetric counter-rotating vortical regions can be observed at the two sides of the wake of the tower, which reveal the presence of a horseshoe vortex system, whose vorticity on the right (respectively, left) part of the domain is enhanced (respectively, inhibited) by the wake rotation. Figure 3 provides the streamwise velocity contours in the (x, y) and (x, z) planes. In the RO case (Figure 3A), the presence of the bottom wall induces a shift of the central high-velocity jet towards the upper part of the wake, as clearly shown in the top left frame. Moreover, the jet persists for more than three diameters behind the rotor. Further downstream, the velocity gradient is smoothed out by the viscosity and the breakdown of the root vortex. Figure 3B shows that, in the TN case, the velocity jet at the center of the rotor is reduced in intensity and length, and both the asymmetry of the wake and the recovery of the wake, especially in its upper part, are enhanced. The wake asymmetry in the horizontal (x, z) planes (bottom frames), in the RO case is due to the wall blockage effect. In the TN case, the low-momentum fluid is lifted up from the tower wake and captured by the rotor wake in the near-wake region; then, this velocity deficit is transported downstream following the rotation of the flow around the axis of the turbine. Therefore, due to the rotation of the wake, the left part

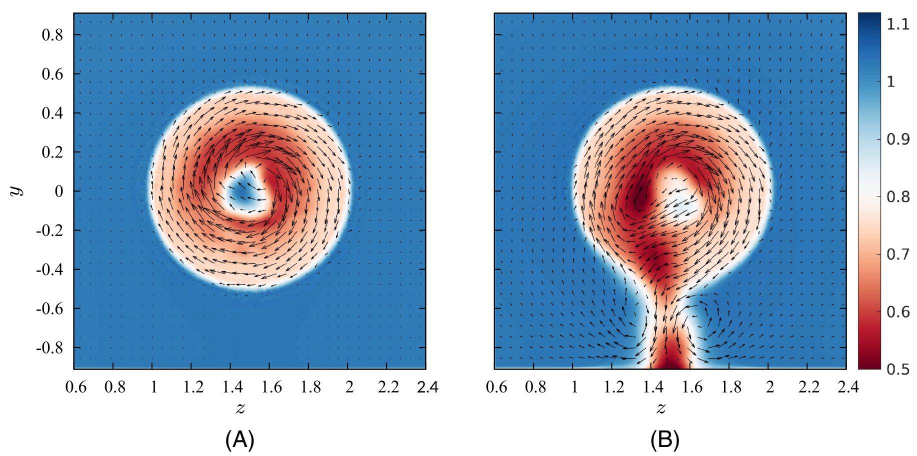

FIGURE 2 Time-averaged streamwise velocity contours at $x = 1$ for the rotor-only case (A) and the tower and nacelle case (B) [Colour figure can be viewed at wileyonlinelibrary.com]

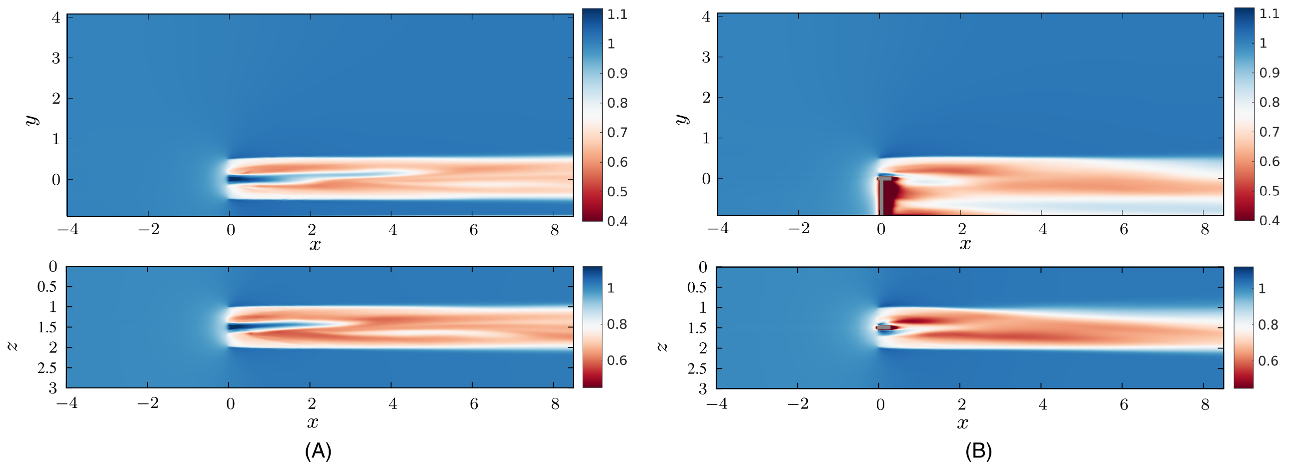

FIGURE 3 Time-averaged streamwise velocity contours in the $x-y$ plane (top frames) and in the $x-z$ plane (bottom frames) passing through the rotor axis for the rotor-only case (A) and the tower and nacelle case (B) [Colour figure can be viewed at wileyonlinelibrary.com]

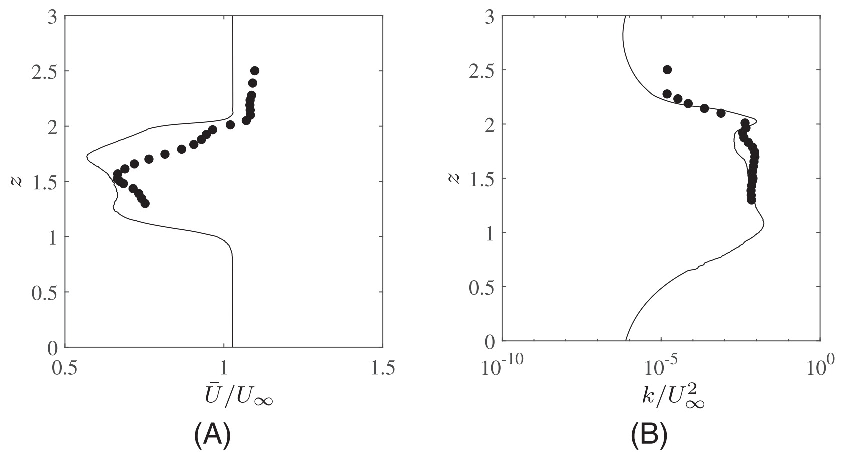

FIGURE 4 Mean streamwise velocity profiles (A) and turbulent kinetic energy profiles (B) at $X/D=3$ and $Y/D=0$: experimental results by Krogstad and Eriksen[45] (———) and large eddy simulation results (●)

of the near wake in Figure 3B shows a lower streamwise velocity and the wake is inclined with respect to the axial direction. In the far-wake region, the recovery of the wake appears enhanced with respect to the RO case.

A qualitative comparison with the experimental data of Krogstad and Eriksen[45] is provided in Figure 4, which shows the mean axial velocity and turbulent kinetic energy profiles along a line at $x=3$ and $y=0$ calculated by LES in the presence of tower and nacelle, compared with the corresponding measured profiles. Numerical and experimental data are in reasonable agreement, considering that their layout geometry is not perfectly coincident. In fact, we recall that the exact experimental conditions were reproduced with the same numerical code used here by Santoni et al.,[34] and the numerical results agreed well with measurements. Whereas, in the present configuration, due to the differences between the numerical and experimental setup (viz., the absence of lateral walls, the increased wall-normal domain, and the decreased dimensions of tower and nacelle), the experimental velocity profile shows a lower deficit within the wake and a higher velocity outside it.

This depends mainly on the domain cross-sectional area: the blockage ratio of the experiment is quite high (13%), larger than that used in our simulation (5%), and this induces a higher acceleration around the turbine. Instead, the computed turbulent kinetic energy profile is in close agreement with the measured one. Finally, Figure 5 shows the averaged velocity distribution in the rotor swept area along the streamwise direction. The averaged velocity drops across the rotor ($X/D=0$), due to the drag force of the turbine, and further downstream in the wake, the velocity increases (wake recovery).

One can observe that the presence of the tower and nacelle (corresponding to the dashed line) on one hand increases the velocity deficit behind the rotor, with respect to the RO case (solid line), and, on the other hand, accelerates the wake recovery by increasing the entrainment of the MKE.

4.2 | Phase-averaged velocity fields

Since the flow under investigation is mainly forced at the frequency corresponding to the rotational speed of the rotor, it is possible to apply a triple decomposition of the turbulent velocity field,[51]

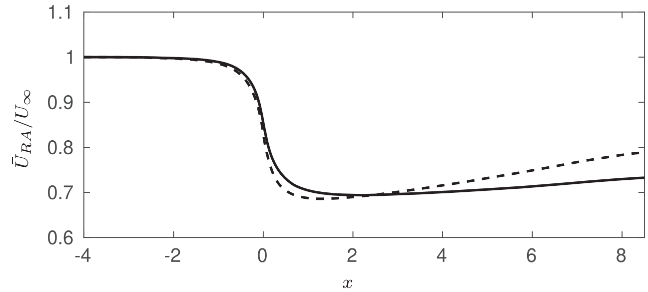

FIGURE 5 Mean streamwise velocity averaged on a disk of radius $R = 0.5$, centered on the rotor axis. Solid line (———) is relative to the rotor-only case, whereas dashed line (– – – –) is relative to the case with tower and nacelle

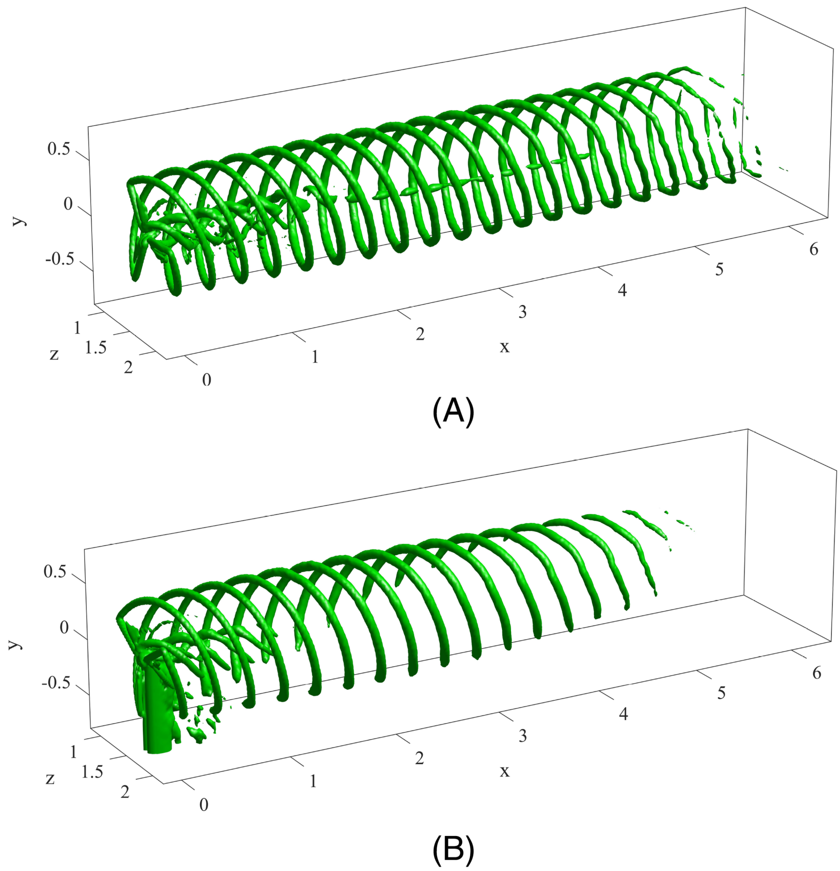

FIGURE 6 Q-criterion isosurfaces ($Q = 5.1$) of the phase-averaged flow fields for the rotor-only (A) and tower and nacelle (B) cases [Colour figure can be viewed at wileyonlinelibrary.com]

$$\boldsymbol{u}(x,y,z,t) = \bar{\boldsymbol{u}}(x,y,z) + \tilde{\boldsymbol{u}}(x,y,z,t_r) + \boldsymbol{u}'(x,y,z,t) \tag{4}$$

where -$\boldsymbol{u}$ is the time-averaged velocity, $\tilde{\boldsymbol{u}}$ is the "coherent" fluctuation with period T dependent on the forcing, $t_r \in [0,T)$, and $\boldsymbol{u}'$ is the "random" fluctuation. We define the coherent fluctuation as $\tilde{\boldsymbol{u}} = \langle \boldsymbol{u} \rangle - \bar{\boldsymbol{u}}$, where $\langle \boldsymbol{u} \rangle$ is the phase-averaged velocity at the Strouhal number of the rotor St_r,

$$\begin{aligned} \langle \boldsymbol{u} \rangle(\mathbf{x},t_r) &= \frac{1}{N}\sum_{n=0}^{N-1} \boldsymbol{u}(\mathbf{x},t_r+nT), \\ T &= \frac{1}{St_r}, \end{aligned} \tag{5}$$

all the remaining part of the perturbation with respect to the time-average flow being included in the random fluctuation $\boldsymbol{u}'$. In both RO and TN cases, the phase-averaged flow fields provided in Figure 6 show quite intense coherent vortical structures shed by the turbine, corresponding to tip and root vortices, as expected. For a three-bladed rotor, the vortical structures oscillate at a characteristic angular frequency, ω_{TV} (where the subscript TV stands for tip vortices), equal to three times the rotor angular frequency Ω. Inspecting closely the isosurfaces of the Q-criterion provided in Figure 6, one can see that, if tower and nacelle are not taken into account, helical tip vortices are advected downstream, almost undisturbed, up to six diameters past the turbine. If, instead, tower and nacelle are included in the simulation, the tip vortices break down earlier,

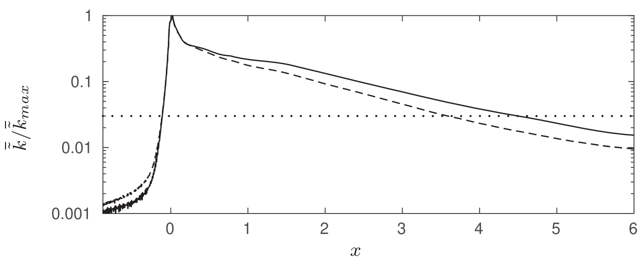

FIGURE 7 Mean kinetic energy of the coherent fluctuation $\tilde{\boldsymbol{u}}$ averaged in $y-z$ planes for each x location, normalized by its maximum. The solid line (———) refers to the rotor-only case, whereas the dashed line (– – – –) refers to the tower and nacelle case. The dotted line (·········) at 0.03 is chosen as the threshold to discriminate near-wake and far-wake regions

mainly at the bottom and left side of the wake. This is due to the interaction with the vortical structures shed by tower and nacelle, which are advected to the left side of the wake by the rotating flow induced by the blades,[34] whereas the tip vortices in the top/right part of the wake are only slightly affected by the presence of tower and nacelle, showing a behavior similar to the RO case. The analysis of the phase-locked fluctuation $\tilde{\boldsymbol{u}}$ allows us to define a criterion for setting apart the near wake from the far wake, which will be used in the next section for the POD analysis. Usually, the distinction between near and far wake is qualitative: the near wake is the region just behind the rotor where the dynamics of the flow is determined by the geometry and working conditions of the rotor itself, namely, by the number of blades, blade aerodynamics, tip vortices, and rotational speed. The far wake is the region beyond the near wake, where the structures linked to the blades' aerodynamics are no longer visible and the flow is dominated by convection and turbulence diffusion.[52]

Several criteria have been employed for the discrimination between near and far wake, for example, the starting location of the wake breakdown[53] or the location where a fully developed Gaussian velocity profile is attained.[54] However, there is not a unified criterion for such a discrimination. The criterion defined and employed in the present work is based on the time-averaged coherent kinetic energy computed as

$$\bar{\bar{k}} = \frac{1}{2}\bar{\tilde{\boldsymbol{u}}}^2, \tag{6}$$

averaged on the $y-z$ planes at each streamwise location. Figure 7 shows the streamwise variation of this quantity (normalized with respect to its maximum value), which decreases in the streamwise direction as the energy passes from coherent to random fluctuations, going from the near to the far wake. The streamwise location at which the value of the coherent averaged kinetic energy drops below 3% of its maximum will be taken hereafter as the threshold between the near- and the far-wake region. Such a criterion, despite being arbitrary by the choice of a threshold value, is closely related to the general definition of near wake, characterized by coherent structures generated by the rotor, in particular by the tip vortex helices, and has proved to be suitable for separating the two flow regions characterized by a different dynamics.

5 | PROPER ORTHOGONAL DECOMPOSITION

The coherent structures developing in the wake of the considered wind turbine are analyzed using POD. This technique allows one to decompose the unsteady flow field into a set of orthonormal functions $\boldsymbol{\phi}_j$, providing a complete basis for each realization of the stochastic process $\boldsymbol{q}(\boldsymbol{x},t)$, which can be expanded as

$$\boldsymbol{q}(\boldsymbol{x},t) = \sum_{j=1}^{\infty} a_j(t)\boldsymbol{\phi}_j(\boldsymbol{x}), \tag{7}$$

with $a_j(t) = \langle \boldsymbol{q}(\boldsymbol{x},t), \boldsymbol{\phi}_j(\boldsymbol{x})\rangle$ being the time coefficients of the expansion. The spatial modes $\boldsymbol{\phi}(\boldsymbol{x})$ are chosen so as to maximize the quantity:

$$\lambda = \frac{E\{|\langle \boldsymbol{q}(\boldsymbol{x},t), \boldsymbol{\phi}(\boldsymbol{x})\rangle|^2\}}{\langle \boldsymbol{\phi}(\boldsymbol{x}), \boldsymbol{\phi}(\boldsymbol{x})\rangle}, \tag{8}$$

where $\langle\cdot,\cdot\rangle$ denotes the inner product and $E\{\cdot\}$ is the expectation operator. Further details on the POD method can be found in Appendix A2.

5.1 | RO case

POD of the flow field in the RO configuration has been carried out over a dataset made of $M = 2575$ snapshots, after validation of the convergence of the POD modes with respect to the number of snapshots. Since the Δt between the different snapshots allows for a 10° rotation of the rotor, 36 snapshots correspond to a complete rotation of the rotor. Therefore, the dataset spans about 71 revolutions. The choice of the snapshots' sampling frequency is justified in Appendix A2. Two different subdomains have been considered, namely, a near-wake (NW) domain and a far-wake (FW) domain. According to the criterion established in the previous section for the near/far wake discrimination, the resulting subdomain extents are $[04.5]\times[-0.80.9]\times[0.32.7]$ for the near wake and $[4.58.4]\times[-0.80.9]\times[0.32.7]$ for the far wake, in x, y, and z directions, respectively. The results of the analyses are nonetheless robust with respect to the choice of the threshold for determining the near- and far-wake regions. In both regions, the velocities have been downsampled with a 1:5 ratio with respect to the computational grid. The POD method ranks the eigenvectors with respect to their energy content, as shown in Figure 8. The top frames of this figure show the flow energy captured by each of the main POD modes expressed as a percentage of the reconstructed total turbulent kinetic energy, computed as $\mathcal{E}=\sum_{i=1}^{M}\lambda_k$, in the near- (left) and far-wake (right) region (the bottom frames showing the same quantities for the TN case). Although the snapshots' matrix is full rank, the POD modes with k greater than those shown in the figure have a slowly decaying energy and an increasingly small-scale disorganized structure, being therefore of little interest for the present study. In all cases, the 0^{th} POD modes (see the left columns of Table 1) are omitted since they simply provide the time average of the instantaneous flow fields.

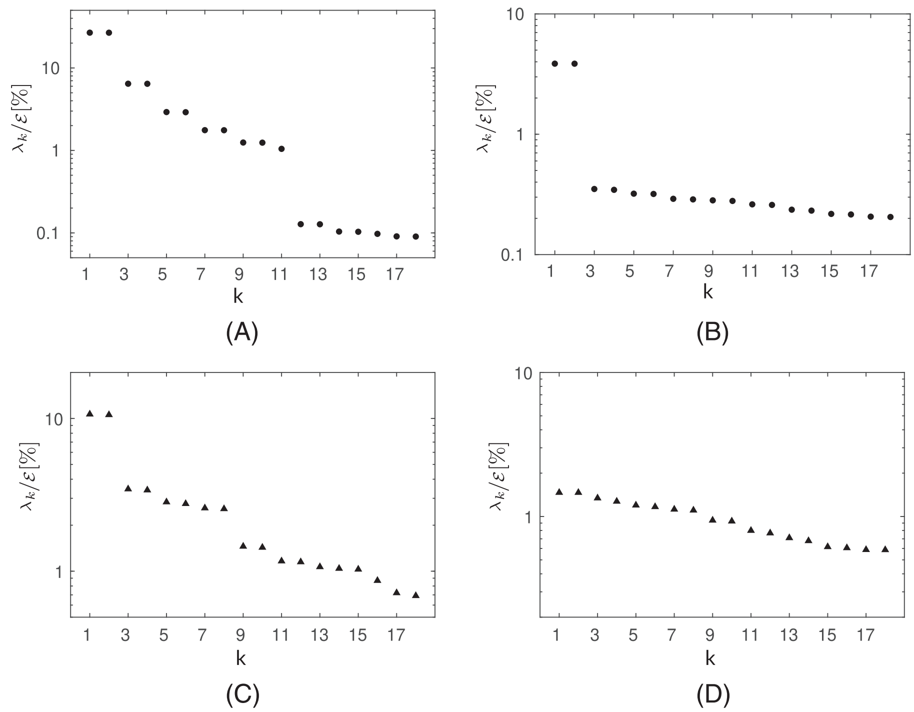

FIGURE 8 Energy of the main proper orthogonal decomposition modes, expressed as a percentage of the total turbulent kinetic energy $\mathcal{E}=\sum_{i=1}^{M}\lambda_k$, for the rotor-only (top) and tower and nacelle (bottom) configuration in the near wake (left) and in the far wake (right)

TABLE 1 Mode number of the rotor-only (top) and tower and nacelle (bottom) cases, according to Figure 8 and leading Strouhal number St_l of the most energetic POD pairs

	Near-wake			Far-wake		
	Pair	**POD modes**	**St_l**	**Pair**	**POD modes**	**St_l**
	RONW0	0	0	ROFW0	0	0
Rotor-only	RONW1	1–2	2.865	ROFW1	1–2	2.865
case	RONW2	3–4	5.73	ROFW2	3–4	1.277
	RONW3	5–6	8.59	ROFW3	5–6	0.883
	RONW4	7–8	11.46	ROFW4	7–8	0.78–1.41
	TNNW0	0	0	TNFW0	0	0
Tower and nacelle	TNNW1	1–2	2.865	TNFW1	1–2	0.883
case	TNNW2	3–4	1.891	TNFW2	3–4	0.246
	TNNW3	5–6	1.03	TNFW3	5–6	0.662
	TNNW4	7–8	5.73	TNFW4	7–8	0.451
	TNNW5	9–10	1.43–0.93	TNFW5	9–10	0.491

Abbreviation: POD, proper orthogonal decomposition.

5.1.1 | Near wake

The most energetic POD modes from 1 to 12 are paired as described in Table 1, since their associated eigenvalues, λ_i, are very close to each other and their time coefficients, $a_i(t)$, have almost identical frequency spectra, as shown in Figure 9A. The first pair of modes, labeled RONW1 and containing about 25% of the total energy, represents the root and tip vortices shed by the blades, as shown in Figure 10 by the combination of the first three POD modes providing the coherent tip and root vortex system together with the central jet due to the absence of the nacelle. The frequency spectra of the time coefficients $a_{2-3}(t)$ related to these modes show, indeed, a single peak at $St_{TV} = \omega_{TV}/2\pi \approx 2.865$, which is three times the Strouhal number correspondent to the rotor angular frequency St_r. This particular value of the Strouhal number is related to the pitch λ_x of the tip and root vortices by the convection velocity of the vortex system. By measuring the pitch λ_x leading to the streamwise wavenumbers $\alpha_{tip} = 2\pi/\lambda_x \approx 20.92$ and $\alpha_{root} \approx 20.36$, the convection velocities of the tip and root vortices can be estimated as $C_{tip} = 2\pi St_{TV}/\alpha_{tip} \approx 0.861$ and $C_{root} \approx 0.88$, where the slightly larger convection velocity estimated for the root vortices is probably due to the presence of a jet at the center of the rotor. The successive mode pairs characterizing the near-wake region are simply harmonics of the first pair. Figure 9A provides the frequency spectra of pairs RONW2/3/4, all of them showing a single peak at values of the Strouhal number multiple of St_{TV}.

5.1.2 | Far wake

In the far-wake region, the first three POD modes are similar to the first three modes found in the near wake. Figure 11 provides the streamwise velocity contours of the pair ROFW1 (where both modes, taken at $t = 0$, have been summed up for the sake of visualization) in the $x-y$ plane containing the rotor axis, showing a clear set of tip vortices fading out towards the end of the domain. The successive pairs of modes instead capture the convective instabilities developing in the far wake and have lower frequencies both in space and time, as shown by the spectra in Figure 9B.

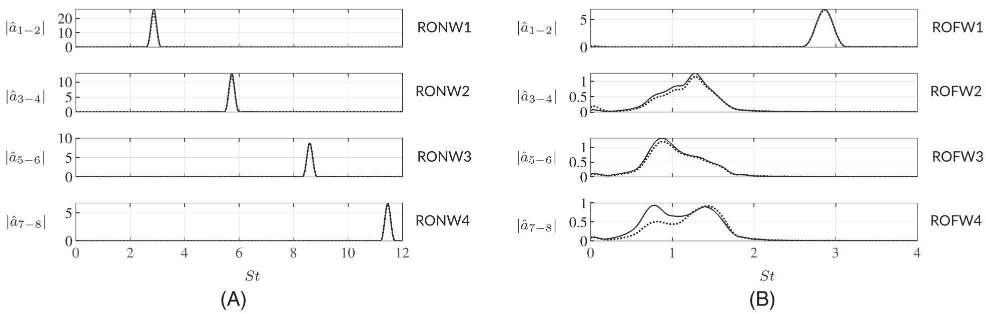

FIGURE 9 Amplitude spectra of time coefficients associated to the first four proper orthogonal decomposition pairs for the rotor-only case in the near wake (A) and in the far wake (B). Solid lines (———) represent the first mode of each pair, whereas dotted lines (-------) represent the second mode

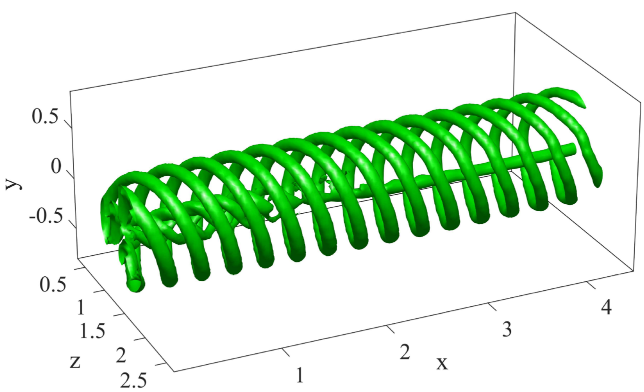

FIGURE 10 Q-criterion isosurface of the velocity field obtained by summing the first three proper orthogonal decomposition modes (RONW0 plus RONW1) multiplied by the corresponding time coefficients at $t = 0$ [Colour figure can be viewed at wileyonlinelibrary.com]

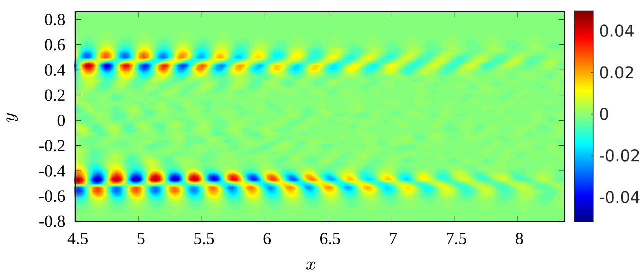

FIGURE 11 Streamwise velocity contours of the ROFW1 pair at $t = 0$ in the $x-y$ plane at $z = 1.5$ [Colour figure can be viewed at wileyonlinelibrary.com]

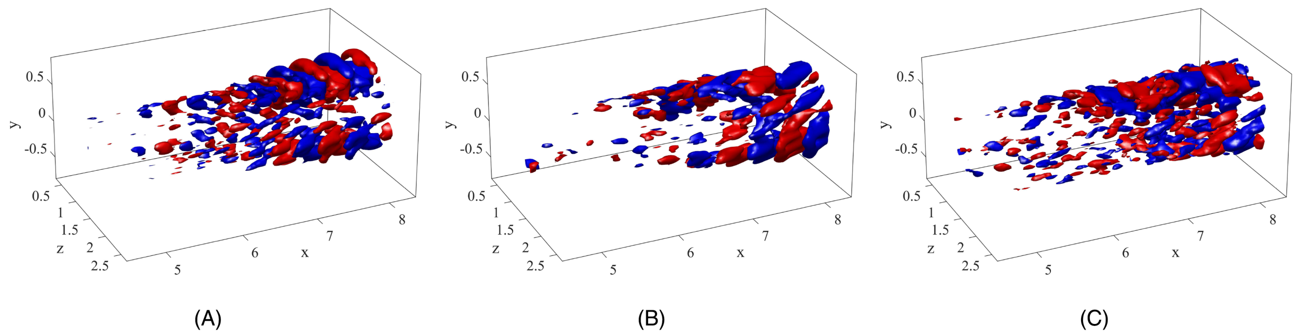

FIGURE 12 Streamwise velocity isosurfaces of the ROFW2 (A), ROFW3 (B), and ROFW4 (C) pairs at $t = 0$ (red for positive, blue for negative values) [Colour figure can be viewed at wileyonlinelibrary.com]

FIGURE 13 Spanwise vorticity contours in the *xy* plane at $z = 1.5$ of the flow field obtained by combining the first five proper orthogonal decomposition modes of the rotor-only case multiplied by the corresponding time coefficients at $t = 0$ [Colour figure can be viewed at wileyonlinelibrary.com]

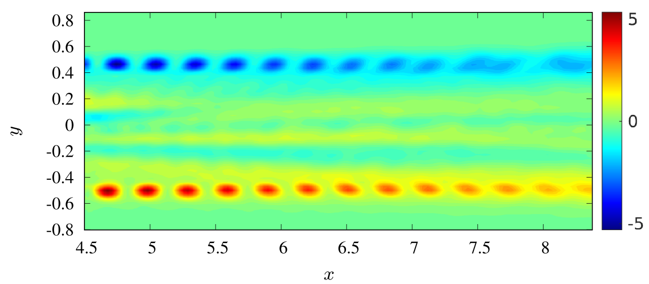

Figure 12 provides the streamwise velocity contours of pairs ROFW2/3/4, showing that they are mostly located in the tip vortex region and, to a lesser extent, in the core of the wake, where radial gradients due to the central jet are present. Looking at the flow field obtained by the combination of the first five POD modes, one can observe a vortex pairing mechanism (see Figure 13 at $x > 6$), recalling the mutual inductance instability phenomenon investigated extensively by Ivanell et al.[16] These authors studied this phenomenon perturbing a steady (low-Re) wake of a wind turbine using low-amplitude excitations located in the neighborhood of the blade tips. They found that the most amplified perturbations are those inducing an out-of-phase displacement of two consecutive vortex spirals.

It has been also shown by Sarmast et al.[15] that the streamwise frequency of the waves responsible for this instability is about half the tip vortices' frequency. Here, the ROFW2 modes have a peak Strouhal number about equal to half the tip vortex one; assuming that these POD pairs are characterized by the same phase velocity, the relation between temporal frequencies is valid also for the streamwise spatial frequencies. Therefore, the ROFW2 pair produces an out-of-phase displacement of two consecutive tip vortices, leading to vortex pairing.

It will be shown in Section 6 that these modes provide an important contribution to the recovery of the wake through MKE entrainment, even though they are about 10 times less energetic than tip vortices, as shown in Figure 8B.

5.2 | TN case

In this section, we discuss the POD results in the flow configuration including the tower and nacelle.

The total number of snapshots considered for the POD is $M = 2361$, stored each 10° rotation for about 65 revolutions. Near- and far-wake subdomains have been considered. According to the criterion described in Section 4.2, the near-wake domain extent is $[0\,3.5] \times [-0.8\,0.9] \times [0.3\,2.7]$ and the far-wake domain extent is $[3.5\,8.4] \times [-0.8\,0.9] \times [0.3\,2.7]$ in *x*, *y*, and *z* directions, respectively. Notice that the near-wake region is shorter than in the RO case. The velocity components, as in the RO configuration, have been downsampled with a ratio 1:5 with respect to the computational grid.

The energy of the main POD modes obtained for the TN configuration in the near wake and in the far wake is provided in the bottom row of Figure 8. The 0^{th} mode is omitted being the time average of the flow, whereas the successive unsteady modes up to the 10^{th} are combined in pairs, according to Table 1. As in the RO case, mode pairing is revealed by the frequency analyses of the corresponding time coefficients, which are provided in Figure 14.

5.2.1 | Near wake

The most energetic POD modes in the near wake for the configuration including tower and nacelle allow us to uncover several important features of the flow. The TNNW1 pair is related to tip and root vortices, as shown in Figure 15A and oscillates at the characteristic Strouhal number of the

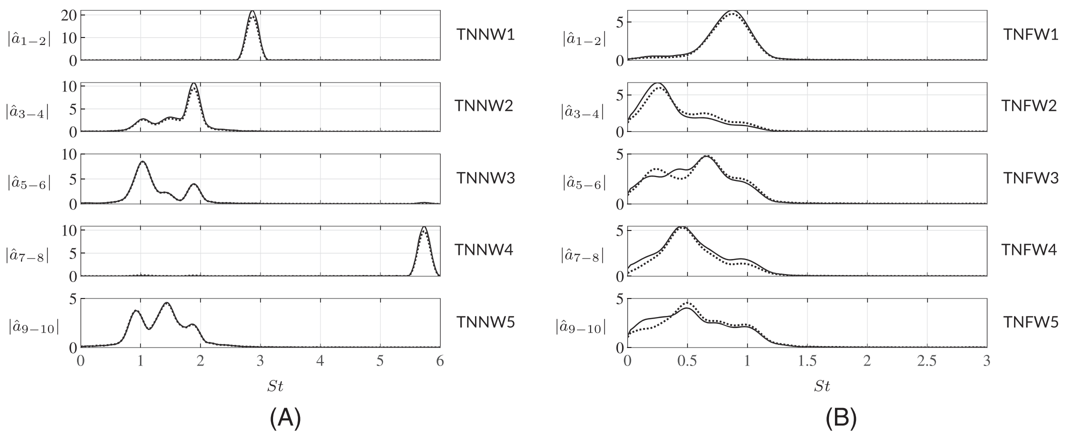

FIGURE 14 Amplitude spectra of time coefficients associated to the first five proper orthogonal decomposition pairs for the tower and nacelle case in the near wake (A) and in the far wake (B). Solid lines (———) represent the first mode of each pair, whereas dotted lines (········) represent the second mode

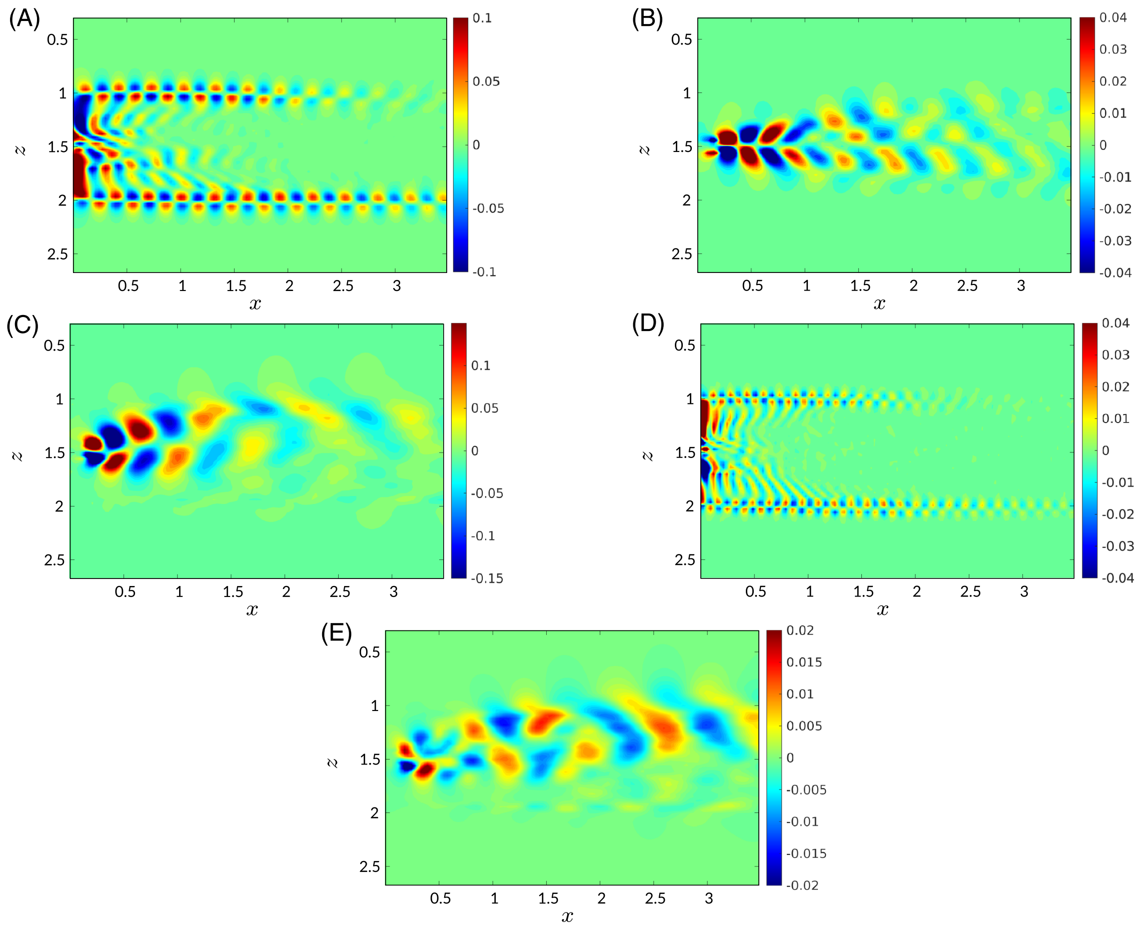

FIGURE 15 Streamwise velocity contours at $t = 0$ of the TNNW1 pair at $y = 0$ (A), TNNW2 pair at $y = -0.5$ (B), TNNW3 pair at $y = -0.3$ (C), TNNW4 pair at $y = 0$ (D), and TNNW5 pair at $y = -0.3$ (E) [Colour figure can be viewed at wileyonlinelibrary.com]

tip vortices St_{TV}, as in the RO case. However, in the present case, these coherent vortical structures are detected by POD mainly on one side of the wake, corresponding to the region where the phase-averaged velocity gradient field discussed in Section 4.2 is stronger. Notice that in this case, the presence of the nacelle induces a reduction of the convection velocity of the root vortices ($C_{root} \approx 0.67$), which translates into a smaller pitch of the root vortices.

The TNNW2 pair provided in Figure 15B is related to the von Karman vortices shed by the tower. It is characterized by a Strouhal number $St \approx 1.891$, which, once rescaled with respect to the tower diameter d_t ($St^* = St(d_t/D) \approx 0.19$), is in close agreement with the value expected for vortices shed by a cylinder of diameter d_t at Reynolds

number $Re_t = Re(d_t/D) = 6.3 \cdot 10^4$. As shown by the 3D visualization in Figure 16A, these vortices are concentrated behind the lower part of the tower, where the velocity hitting the tower is substantially undisturbed and aligned with the streamwise direction. As expected in the case of the vortex shedding behind a cylinder, these vortices propagate downstream in the streamwise direction, but extending in the spanwise one, although not in a homogeneous way due to the intrinsic asymmetry of the mean flow.

The TNNW3 pair provided in Figure 15C can be ascribed as well to the shedding of a von Karman-like vortex street behind the tower. As shown in Figure 16B, this vortex street occupies also the upper part of the tower, where the velocity investing the tower is influenced by rotor blades' passage. As already discussed in Section 4, the mean velocity behind the rotor has a lower magnitude than the undisturbed one and is characterized by a swirling motion opposite to the rotor direction of rotation. This makes the TNNW3 pair oscillate at a lower Strouhal number ($St \approx 1.03$) and propagate in a direction which is slightly inclined with respect to the axial direction towards the left side of the domain. Approximately one to two diameters behind the rotor, the vortex street reaches the edge of the wake and interacts with the tip vortices, causing the breakdown of the spirals and producing a large-scale perturbation which can be observed in Figure 17, where the solid contours of the TNNW3 modes are superimposed on the shaded contours of the TNNW1 pair.

The TNNW4 pair is a harmonic of the first pair, as can be immediately deduced comparing Figures 15A and 15D. Frequency analysis of the relative time coefficients highlights a single peak at $St \approx 5.73$, which is two times the Strouhal number of the tip vortices, St_{TV}. The TNNW5 pair appears less coherent with respect to the first four pairs and it is similar, both in shape and in spectral distribution, to the TNNW3 pair; therefore, it can be related to the same physical mechanism. Despite having a lower energy with respect to preceding pairs, the TNNW5 pair contributes to wake recovery as much as the modes characterized by higher energy, as it will be shown in Section 6.

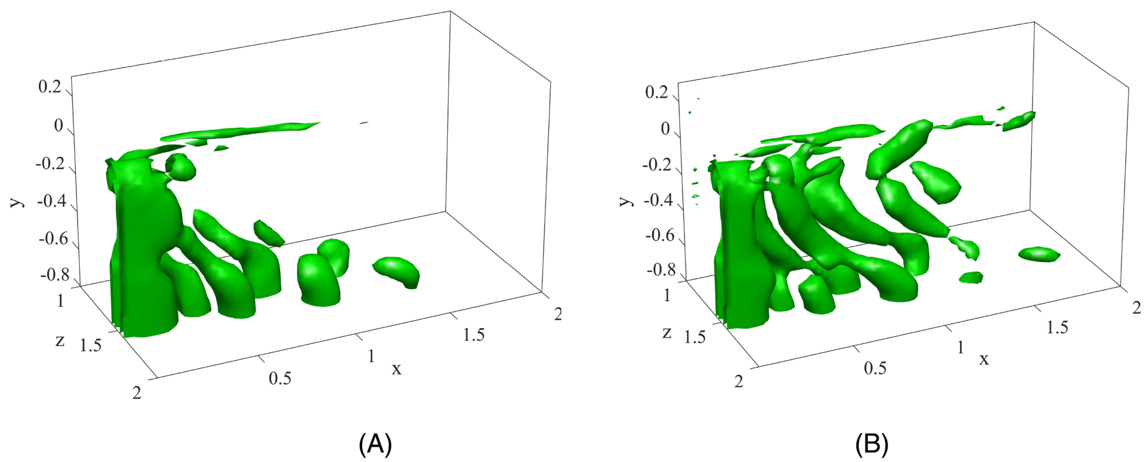

FIGURE 16 Q-criterion isosurfaces obtained by summing mode TNNW0 to the TNNW2 (A) and the TNNW3 (B) proper orthogonal decomposition pairs in the near-wake region [Colour figure can be viewed at wileyonlinelibrary.com]

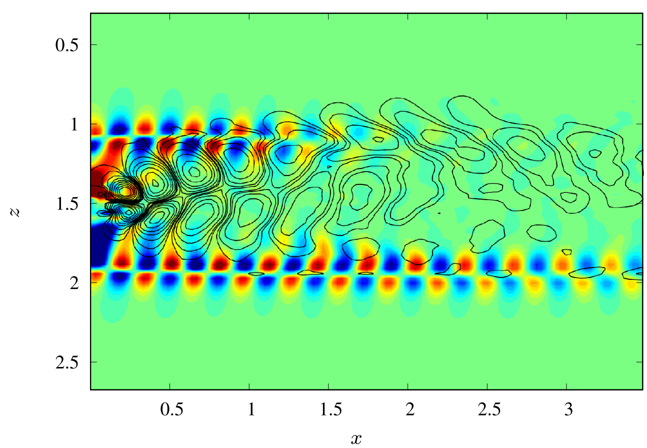

FIGURE 17 Streamwise velocity contours at $t = 0$ for the TNNW3 pair (solid contours) superimposed to the TNNW1 pair at $y = -0.3$ (shaded ones) [Colour figure can be viewed at wileyonlinelibrary.com]

5.2.2 | Far wake

In contrast to all other cases, POD analysis of the far-wake flow field in the TN configuration shows that the most energetic perturbations are not associated with the tip and root vortices. The TNFW1 pair, provided in Figure 18A, is characterized by a structure similar to the TNNW3 pair in the region farther from the turbine. Also, their Strouhal numbers are similar, although the TNNW3 one is slightly higher, probably due to the presence of higher frequency oscillations close to the turbine. This suggests that these two coherent structures detected in the near and far wake may represent the same perturbation that originates just behind the rotor and reduces its frequency while propagating downstream and interacting with tip vortex spirals. These highly energetic and dynamically relevant POD modes, together with the TNNW2/5 pairs, were totally undetected in the RO configuration. This indicates the crucial role of the turbine's tower, which strongly influences the wake both in the near- and in the far-wake region as it will be discussed in detail in Section 6.

The successive pair of modes, TNFW2, is characterized by spatial oscillation of larger wavelength, as shown in Figure 18B. Both modes of this pair oscillate at an even lower frequency than the previous ones, having $St \approx 0.246$. This frequency lies within the frequency range typical of the wake meandering.[55-57] In this case, this low-frequency oscillation is clearly not induced by atmospheric eddies. Rather, in the present case, nonlinear interactions between rotor and tower vortices play an important role in their generation. In fact, the TNFW2 pair is mostly concentrated on the left side of the wake, where the vortices shed by the tower hit the tip vortices spirals leading to their breakdown.

The successive modes have a broader spectrum and a more disorganized spatial structure as can be observed from Figures 14B and 18C–E. The TNFW4/5 pairs might be harmonics of TNFW2, since their peak Strouhal number is approximately two times that of the TNFW2 pair (see Table 1). One can also notice that they are more concentrated on the left side of the wake. Instead, in the flow region where the tip vortices are not broken (top/right side of the domain), the wake remains substantially straight, without strong oscillations. This confirms the crucial importance of simulating the presence of tower and nacelle for accurately describing the wake dynamics and suggests that, in the present case, convective linear instabilities of tip vortices spirals, if present, are energetically less important than the oscillations produced by tower and nacelle.

5.3 | Comparison of the RO and TN cases

As a summary of the presented results, Figure 19 provides a bar plot of the Strouhal numbers of the main POD modes in the four considered cases, RONW, ROFW, TNNW, and TNFW. One can notice that POD modes characterized by Strouhal number $St_f \approx 2.865$ and composed by tip and root vortices (RONW1, ROFW1, and TNNW1) are found in all considered cases but the TNFW one. In fact, in the near wake, the tip and root

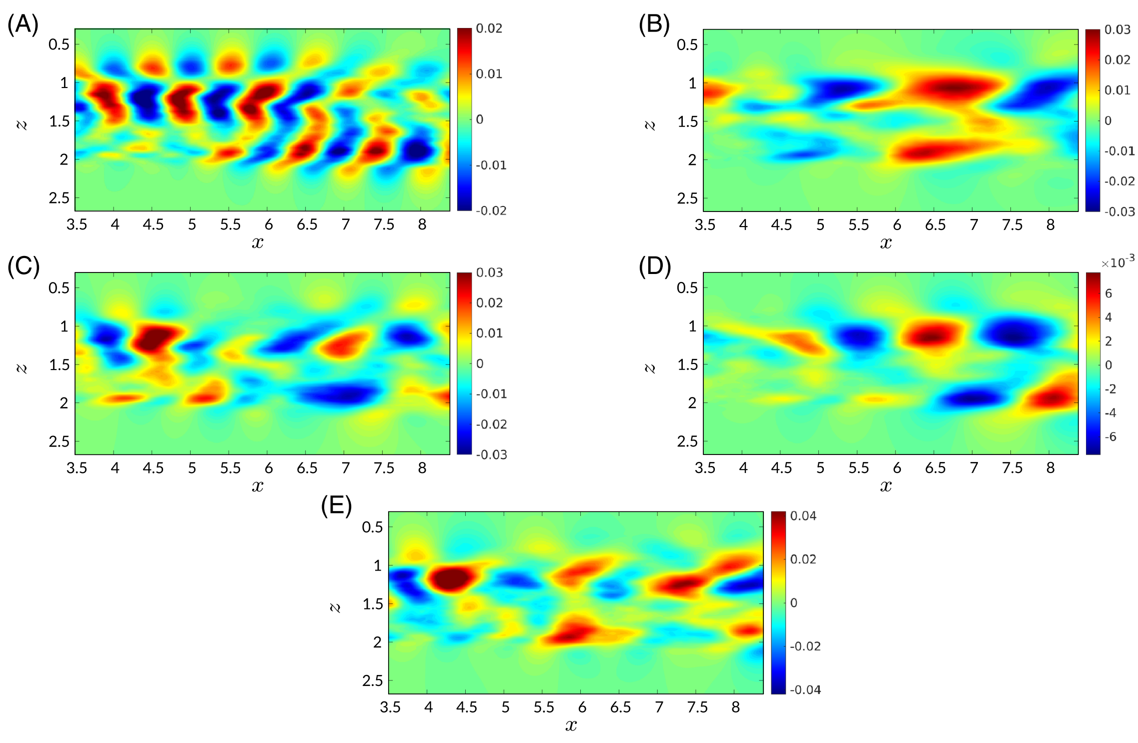

FIGURE 18 Streamwise velocity contours at $y = -0.3$ and $t = 0$ of the TNFW1 pair (A), TNFW2 pair (B), TNFW3 pair (C), TNFW4 (D), and TNFW5 (E) [Colour figure can be viewed at wileyonlinelibrary.com]

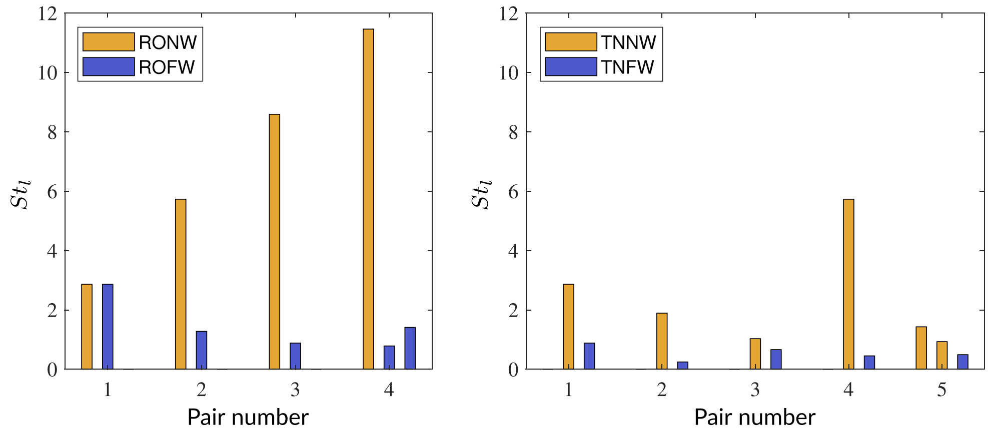

(A) RO (B) TN

FIGURE 19 Leading Strouhal numbers St_l of the most energetic proper orthogonal decomposition pairs of the rotor-only (left) and tower and nacelle (right) cases [Colour figure can be viewed at wileyonlinelibrary.com]

vortex system appears to be only slightly affected by the presence of the tower and nacelle, whereas in the far wake, the presence of tower and nacelle is found to promote the breakdown of the tip vortices, enhancing wake recovery (as it will be further discussed in Section 6), explaining why the frequency typical of tip vortices is not found among the most energetic ones in the TNFW case. Similar conclusions can be drawn for all the POD modes that are dynamically linked to the tip and root vortices, for instance, the RONW2 and TNNW4 modes which represent the first harmonic of the tip vortices ($St = 5.73 \approx 2 \times 2.865$).

The robustness of the modes linked to the tip vortices with regard to the presence or absence of tower and nacelle explains most of the consistencies between frequencies in the different considered cases. The only exception are the ROFW3 and TNFW1 modes, which are associated to very similar Strouhal number by mere coincidence, since these modes have a very different spatial support being connected to different physical mechanisms. In particular, the ROFW3 pair develops symmetrically throughout the azimuthal direction in the region of the tip vortices, being connected to their convective instability, whereas the TNFW1 is mostly located in the bottom-left region of the wake, with a pronounced asymmetry, being attributed to nonlinear interaction between the tip vortices and the wake of the tower. Figure 19 clearly shows that the energy is differently distributed between the modes depending on the presence (or not) of tower and nacelle. For instance, in the TN case, the first harmonic of the tip vortices (mode pair 4) has a lower energetic content with respect to other emerging modes. Moreover, new low-frequency POD modes emerge that overtake in energy those connected with the tip vortices dynamics. These modes characterized by very low frequencies typical of wake meandering (TNFW2) remained completely undetected by the POD analysis in the RO cases. In the next section, these modes will be shown to have a positive impact on wake recovery. Thus, the direct comparison of the energy and frequency content of the coherent structures in the RO and TN cases clearly indicates that despite a few similarities, several important differences can be detected in the POD modes recovered in these two cases. These results point out that for accurately describing the flow dynamics, POD analysis of coherent structures should be made in the presence of tower and nacelle, as well as on sufficiently long computational domains, in order to capture the low-frequency POD modes typical of the far wake.

6 | MKE ENTRAINMENT

It is well established that the larger the turbulence intensity of the flow approaching the turbine, the higher the wake recovery rate. In fact, the transport of MKE within the wake is enhanced by the diffusion provided by the turbulent fluctuations. However, through quadrant analysis, Lignarolo et al.[58] showed that tip vortices do not provide any contributions to the overall turbulent mixing. Medici[55] reported even a shielding effect of the tip vortices, which prevent the near-wake shear layer to recover. To assess this hypothesis, we evaluate the contribution of each POD mode to wake recovery using the following transport equation for the MKE:

$$
\begin{aligned}
0 = & -\bar{u}_j \frac{\partial}{\partial x_j}\left(\frac{1}{2}\bar{u}_i\bar{u}_i\right) - \frac{\partial}{\partial x_i}(\bar{u}_i p^*) + \bar{u}_i\bar{F}_i + \frac{1}{Re}\nabla^2\left(\frac{1}{2}\bar{u}_i\bar{u}_i\right) - \frac{1}{Re}\frac{\partial \bar{u}_i}{\partial x_j}\frac{\partial \bar{u}_i}{\partial x_j} + \\
& \underbrace{-\frac{\partial}{\partial x_j}\left(\bar{u}_i\overline{u_i' u_j'}\right) - \frac{\partial}{\partial x_j}\left(\bar{u}_i\overline{\tau^r_{ij}}\right)}_{\text{Turbulent MKE flux}} + \overline{u_i' u_j'}\frac{\partial \bar{u}_i}{\partial x_j} + \overline{\tau^r_{ij}}\frac{\partial \bar{u}_i}{\partial x_j}.
\end{aligned} \tag{9}
$$

It is known that the turbulent MKE flux, highlighted in Equation (9), is the term that mostly contributes to wake recovery.[14,34,59] Moreover, in the wake region, the subgrid-scale stresses are negligible with respect to the Reynolds stress terms; therefore, in this analysis, their contribution to the turbulent MKE flux is neglected. The total flux of MKE per unit area due to turbulent fluctuations through a generic closed surface can be evaluated, using the Gauss theorem, by the following equation:

$$\mathcal{F}_T = \frac{1}{S}\int_V -\frac{\partial}{\partial x_j}(\bar{u}_i \overline{u'_i u'_j})dV, \tag{10}$$

where V is the volume enclosed by the surface S. Note that, by the above definition, the energy flux entering the volume is positive. Given the POD properties described in Section A2, the Reynolds stress tensor can be decomposed as

$$\overline{u'_i u'_j} = \overline{\sum_{k=1}^{N}(a_k \phi_i^k)\sum_{l=1}^{N}(a_l \phi_j^l)} = \sum_{k=1}^{N}\sum_{l=1}^{N}\overline{a_k a_l}\phi_i^k \phi_j^l = \sum_{k=1}^{N}\lambda_k \phi_i^k \phi_j^k. \tag{11}$$

Therefore, using this decomposition, we can compute the contribution of each POD mode to the turbulent MKE flux as

$$\mathcal{F}_T^k = \frac{1}{S}\int_V -\frac{\partial}{\partial x_j}(\bar{u}_i \lambda_k \phi_i^k \phi_j^k)dV. \tag{12}$$

The last equation can be rewritten as a surface integral:

$$\mathcal{F}_T^k = \frac{1}{S}\int_S -\bar{u}_i \lambda_k \phi_i^k \phi_j^k dS_j. \tag{13}$$

We consider a cylindrical domain of radius R_c and length L_c centered on the rotor axis and we focus on the turbulent MKE flux through its lateral surface. Figure 20 shows the cylindrical domain of radius $R_c = 0.5$ and length L_c equal to the size of the far-wake region. The streamwise velocity isosurfaces of the ROFW3 pair are represented in red and blue, for reference. The vector representing the infinitesimal surface element $\boldsymbol{dS}$ is normal to the streamwise direction; therefore, it can be expressed in Cartesian coordinates as

$$\boldsymbol{dS} = (0, dc_2, dc_3)dx, \tag{14}$$

where dc_2 and dc_3 are the components in the wall-normal and spanwise directions, respectively, of the vector $\boldsymbol{dc}$ normal to the infinitesimal arc of the cylinder circumference C. The total flux per unit area of turbulent MKE for each POD mode over the lateral surface of the cylinder can be calculated as

$$\mathcal{F}_T^k = \int_{L_c} f_T^k(x)dx, \tag{15}$$

$$f_T^k(x) = -\frac{1}{2\pi R_c L_c}\int_C \bar{u}_i(x)\lambda_k \phi_i^k(x)\phi_j^k(x)dc_j. \tag{16}$$

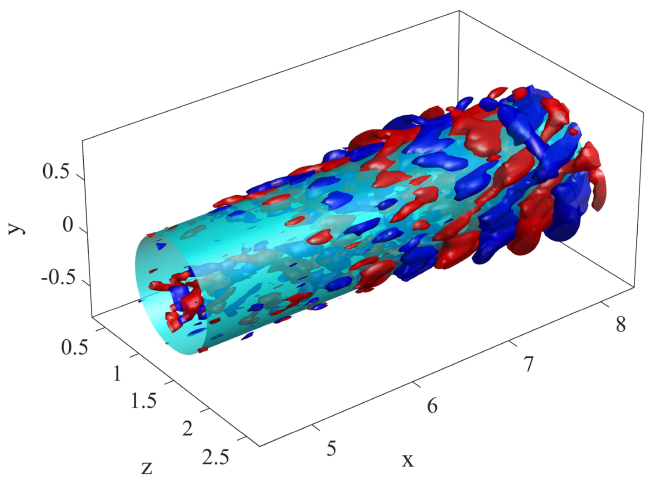

FIGURE 20 Cylindrical domain used for mean kinetic energy flux evaluation in the far-wake region. The red and blue isosurfaces represent the streamwise velocity component of the ROFW3 pair [Colour figure can be viewed at wileyonlinelibrary.com]

The local fluxes $f_T^k(x)$ are computed for a circumference of radius $R_c = 0.5$, whereas the total fluxes $\mathcal{F}_T^k$ through the entire surface are computed for different radii in the range $R_c \in [0.350.62]$. For avoiding a direct computation of the integrals over these cylindrical surfaces, the surface integrals of Equation (16) are transformed, using the divergence theorem, into volume integrals which are then numerically evaluated using the midpoint rule on subintervals of length compatible with the grid size.

Figure 21A shows that all the most energetic POD pairs found in the near-wake region in the RO case, which are directly related to the tip and root vortices, provide mostly negative MKE local flux at $R_c = 0.5$, except for some isolated, small positive peak of the RONW1/2 pairs in the vicinity of the turbine. As shown in Figure 21B, the total flux of all the considered modes is negative for all $R_c \leq 0.5$. Increasing the cylinder radius to $R_c \geq 0.5$, the total flux changes sign and becomes positive at $0.5 < R_c < 0.55$, finally decreasing towards zero for $R_c > 0.62$. This indicates that the tip vortices provide positive MKE flux to an annular region with $0.5 < R_c < 0.55$ that contains the wake shear layer, as we can better observe from Figure 22, showing both the total flux of modes RONW1 and the time-averaged streamwise velocity profile versus R_c. In particular, the radius at which the MKE flux changes its sign corresponds to the region where the mean streamwise velocity radial profile presents an inflection point, suggesting that the mean flow profile is strongly influenced by these modes, which extract energy from the region inside the wake, feeding the mean flow shear layer. Thus, the tip vortices appear to strongly contribute to the sustainment of the wake, which remains almost unchanged in the streamwise direction (see Figure 3A). Therefore, this analysis clearly indicates that the tip vortex system in the near-wake region of the RO case does not contribute to the wake recovery, but rather it tends to sustain the velocity gradient, confirming the findings of Lignarolo et al.[58] Although a direct quantitative comparison with the results of Lignarolo et al.[58] is not possible since those experiments were performed at a lower

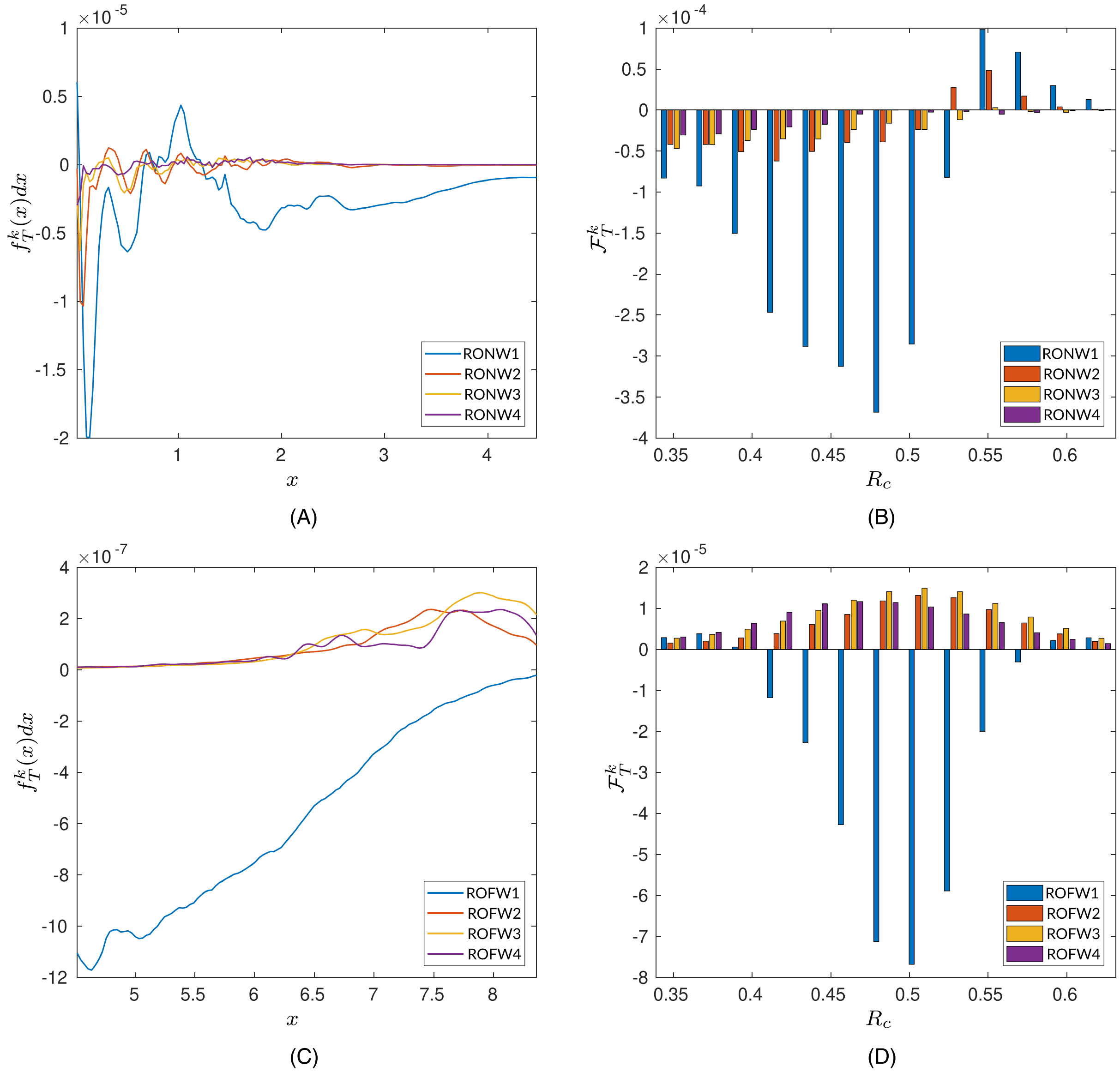

FIGURE 21 Mean kinetic energy entrainment for the rotor-only case: local (A–C) and total (B–D) fluxes, in the near wake (A, B) and in the far wake (C, D) [Colour figure can be viewed at wileyonlinelibrary.com]

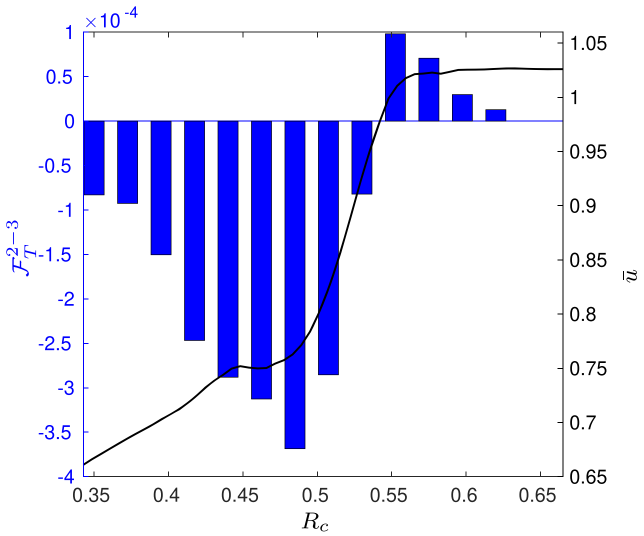

FIGURE 22 Solid line: radial profile of the time-averaged streamwise velocity $\bar{u}$ along an horizontal line at $x = 6.25$, namely, at the center of the near-wake domain for the rotor-only case. Bar chart: total mean kinetic energy flux for the RONW1 pair versus the radius R_c of the cylindrical surface over which the flux is computed [Colour figure can be viewed at wileyonlinelibrary.com]

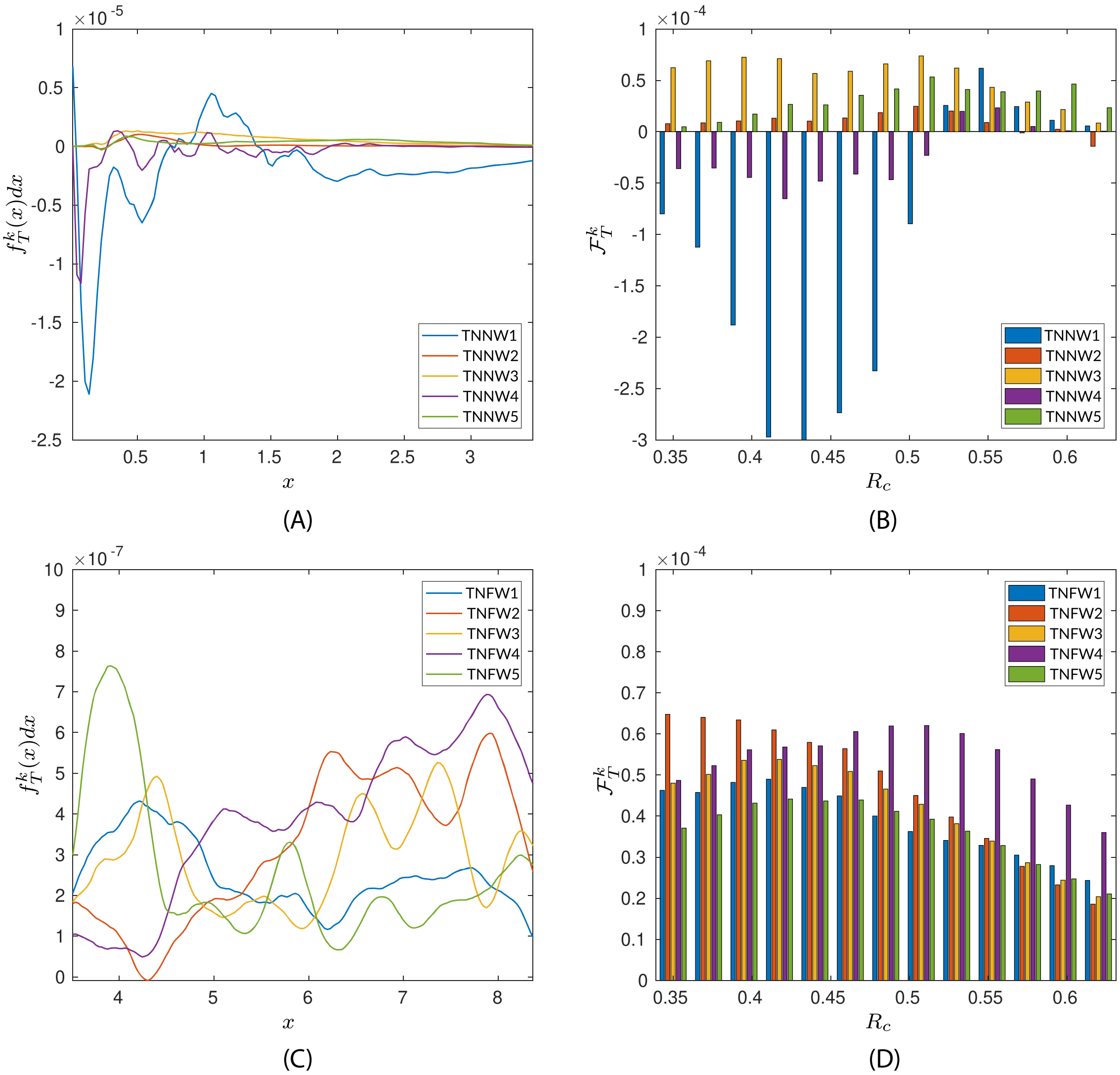

FIGURE 23 Mean kinetic energy entrainment for the tower and nacelle case: local (A–C) and total (B–D) fluxes, in the near wake (A, B) and in the far wake (C, D) [Colour figure can be viewed at wileyonlinelibrary.com]

Reynolds number and a higher tip speed ratio, it appears that the overall scenario of the entrainment is qualitatively very similar. In fact, in the near-wake region, they observe positive and negative contributions of similar magnitude to the energy flux into the wake due to the presence of the tip vortex helix. Further downstream, after the the tip vortex breakdown, a positive flux, corresponding to a net entrainment of kinetic energy into the wake, is observed. In our computations, we have decomposed the energy flux contributions among the POD modes. We have found that the contribution to the energy flux into the wake of the modes associated with the tip vortices (pair 1 in Figure 21C) is always negative and it reduces in modulus with the distance from the rotor. At about $x = 6.5$, it is counterbalanced by the positive flux contribution of modes 2–4 which give a positive entrainment, starting the recovery process of the wake. The abscissa at which the recovery process starts is strongly dependent on the flow condition (Reynolds number and tip speed ratio) and on the interaction with the tower and nacelle wake; in the case studied by Lignarolo et al.,[58] the recovery process starts about at $x = 1.5 - 1.7$, depending on the value of the tip speed ratio.

Concerning the far-wake region of the RO case, the first POD pair (ROFW1), being characterized by tip vortices, presents a negative local MKE flux at $R_c = 0.5$ similarly to the near-wake modes (cf. Figure 21A–C). Moreover, Figure 21D shows that the total MKE flux provided by this mode is negative in the region $0.4 < R_c \leq 0.55$, becoming positive for larger radii, as found for near-wake modes. The other POD pairs instead provide a positive local and total flux, the latter reaching its maximum for $0.5 < R_c < 0.55$, but remaining positive for all considered radii. Therefore, in contrast to the tip vortices, these modes appear beneficial to wake recovery, since they transport the MKE inside the wake.

The same analysis has been performed for the POD pairs found in the TN case. Figure 23A,B shows the MKE local and total fluxes for POD pairs in the near-wake region. The TNNW1 and TNNW4 pairs, which are characterized by tip vortices, behave similarly to the corresponding POD pairs related to tip vortices found in the RO case. The successive modes, as in the far-wake region of the RO case, appear beneficial to wake recovery, providing positive total MKE flux through the cylindrical surfaces for any R_c. In the far-wake region of the TN case, as already observed in Section 5.2.2, tip vortices are not recovered among the most energetic POD modes. As a consequence, Figure 23C,D clearly shows that all of the POD pairs provide positive flux at every radius, thus positively contributing to the mean flow diffusion and to the wake recovery. This analysis suggests that the oscillations generated by the presence of tower and nacelle play a crucial role on wake recovery for three main reasons. The first one is that high-energy modes generated by tower and nacelle are active in the MKE entrainment mechanism from the very near wake, whereas the near wake of the RO case is characterized only by modes that do not contribute positively to the wake recovery. The second reason is that, even in the far wake, the most energetic coherent fluctuations found in the presence of tower and nacelle have a stronger impact on wake recovery with respect to those characterizing the RO case. Comparing Figures 21D and 23D, we can notice that the MKE fluxes measured in the TN case are about three times those calculated for the RO case. The third reason is that the presence of tower and nacelle reduces the shielding effect of tip vortices to wake recovery. Tip vortices break down beforehand due to interactions with coherent structures generated by tower and nacelle, as discussed in detail in Section 5.2.1, leading to the generation of other low-frequency modes, some of those linked to the wake meandering, which are instead beneficial to wake recovery.

7 | CONCLUSIONS

This work provides a detailed analysis of the wake produced by a three-bladed wind turbine and of the main embedded coherent structures, which are identified by means of POD. The analysis is based on LESs of a model wind turbine with an incoming uniform velocity profile at a fixed tip speed ratio $\lambda = 3$. The turbine is simulated with and without tower and nacelle, for evaluating their effect on the wake dynamics. In both cases, rotor blades are modeled using the actuator line method, whereas tower and nacelle are modeled using an immersed boundary method. Time- and phase-averaged flow fields are computed and analyzed, highlighting and comparing the main flow features in the RO and TN cases. In the latter case, the far wake is characterized by a higher velocity on the left side of the turbine, related to a faster overall recovery. Analysis of the phase-averaged RO case flow shows that tip vortices spirals are advected downstream almost undisturbed until the end of the computational domain, whereas in the TN case, breakdown of the tip vortices occurs at the bottom and left side of the wake, suggesting a correlation between the tip vortices breakdown and the increased wake recovery. Based on the evaluation of the kinetic energy of the phase-averaged flow field, we propose a criterion to discriminate the near- from the far-wake region of the flow. The unsteady flow fields are studied separately in these two subdomains (near and far wake) using POD for capturing the energy-containing structures embedded in the turbulent flow. In the RO case, the most energetic POD modes are characterized by tip and root vortices. In the far wake, lower frequency POD modes are recovered, which appear to be linked to a vortex pairing process. In the TN case, in addition to tip and root vortices, highly energetic POD modes connected with the Kármán vortex street developing behind the tower are found as well. These vortical structures originate in the near wake just behind the rotor and are advected towards the left side of the wake, until they interact with and break down the tip vortices on the bottom and left side of the wake. This interaction between tip vortices and tower vortices leads to low-frequency oscillations also in the far wake. In the same region, POD modes characterized by a very low Strouhal number ($St = 0.246$) lying in the typical range of the wake meandering are recovered. These coherent structures appear to be linked to nonlinear interactions of coherent structures generated in the near wake by the presence of the tower.

POD analysis has also been used to investigate in detail the wake recovery process, where turbulent fluctuations play a fundamental role. The effect of each POD mode on wake recovery is evaluated computing its contribution to the MKE entrainment.[14] The MKE flux provided by each POD mode through the surface of a cylinder of radius R_c, centered on the rotor axis, is computed. The flux provided by the tip vortices is negative for small radii and then becomes positive for larger radii. Thus, tip vortices provide positive flux into an annular region containing the wake shear layer, sustaining the mean velocity gradient and slowing down the wake recovery, whereas a positive flux is observed at each radius for POD pairs related to the tower's wake, compensating the shielding effect of the tip vortices and finally enhancing the wake recovery process. These findings indicate the crucial importance of considering tower and nacelle when simulating the flow behind a wind turbine.

Future works will aim at investigating the influence of inlet turbulence on the POD modes. Moreover, it might be also interesting to unravel the mechanism leading to the generation of coherent structures characterized by a low frequency lying in the range of wake meandering.

PEER REVIEW

The peer review history for this article is available at https://publons.com/publon/10.1002/we.2592.

ORCID

Giovanni De Cillis https://orcid.org/0000-0002-0750-5787
Stefano Leonardi https://orcid.org/0000-0002-4570-2255

REFERENCES

1. IEA. Global energy & CO_2 status report 2018. *Tech. Rep.*, International Energy Agency; 2019.
2. REN. Renewable 2019. Market analysis and forecast from 2019 to 2024. *Tech. Rep.*, International Energy Agency; 2019.
3. Barthelmie RJ, Frandsen ST, Nielsen MN, Pryor SC, Rethore P-E, Jørgensen HE. Modelling and measurements of power losses and turbulence intensity in wind turbine wakes at middelgrunden offshore wind farm. *Wind Energy: An Int J Prog Appl Wind Power Convers Technol*. 2007;10(6):517-528.
4. Sanderse B, Van der Pijl SP, Koren B. Review of computational fluid dynamics for wind turbine wake aerodynamics. *Wind Energy*. 2011;14(7):799-819.
5. Stevens RJ, Meneveau C. Flow structure and turbulence in wind farms. *Annu. Rev. Fluid Mech*. 2017;49:311-339.
6. Porté-Agel F, Bastankhah M, Shamsoddin S. Wind-turbine and wind-farm flows: a review. *Bound-Layer Meteorol*. 2019;174:1-59.
7. Hamilton N, Suk Kang H, Meneveau C, Bayoán Cal R. Statistical analysis of kinetic energy entrainment in a model wind turbine array boundary layer. *JRSE*. 2012;4(6):063105.
8. Hussain AF. Coherent structures and turbulence. *J Fluid Mech*. 1986;173:303-356.
9. Speziale CG. On the decomposition of turbulent flow fields for the analysis of coherent structures. *Acta Mech*. 1987;70(1-4):243-250.
10. Lumley JL. *Stochastic Tools in Turbulence*, Applied mathematics and mechanics. Saint Louis: Academic Press; 1970.
11. Sirovich L. Turbulence and the dynamics of coherent structures. Parts I–III. *Q Appl Math*. 1987;45(3):561-590.
12. Berkooz G, Holmes P, Lumley JL. The proper orthogonal decomposition in the analysis of turbulent flows. *Ann Rev Fluid Mech*. 1993;25(1):539-575.
13. Andersen SJ, Sørensen JN, Mikkelsen R. Simulation of the inherent turbulence and wake interaction inside an infinitely long row of wind turbines. *J Turbul*. 2013;14(4):1-24.
14. VerHulst C, Meneveau C. Large eddy simulation study of the kinetic energy entrainment by energetic turbulent flow structures in large wind farms. *Phys Fluids*. 2014;26(2):025113.
15. Sarmast S, Dadfar R, Mikkelsen RF, Schlatter P, Ivanell S, Sørensen JN, Henningson DS. Mutual inductance instability of the tip vortices behind a wind turbine. *J Fluid Mech*. 2014;755:705-731.
16. Ivanell S, Mikkelsen R, Sørensen JN, Henningson D. Stability analysis of the tip vortices of a wind turbine. *Wind Energy*. 2010;13(8):705-715.
17. Bastine D, Witha B, Wächter M, Peinke J. Towards a simplified dynamic wake model using pod analysis. *Energies*. 2015;8(2):895-920.
18. Hamilton N, Tutkun M, Cal RB. Wind turbine boundary layer arrays for Cartesian and staggered configurations: part II, low-dimensional representations via the proper orthogonal decomposition. *Wind Energy*. 2015;18(2):297-315.
19. Hamilton N, Tutkun M, Cal RB. Anisotropic character of low-order turbulent flow descriptions through the proper orthogonal decomposition. *Phys Rev Fluids*. 2017;2:014601. https://doi.org/10.1103/PhysRevFluids.2.014601
20. Hamilton N, Tutkun M, Cal RB. Low-order representations of the canonical wind turbine array boundary layer via double proper orthogonal decomposition. *Phys Fluids*. 2016;28(2):025103. https://doi.org/10.1063/1.4940659
21. Hamilton N, Viggiano B, Calaf M, Tutkun M, Cal RB. A generalized framework for reduced-order modeling of a wind turbine wake. *Wind Energy*. 2018; 21(6):373-390.
22. Ali N, Cortina G, Hamilton N, Calaf M, Cal RB. Turbulence characteristics of a thermally stratified wind turbine array boundary layer via proper orthogonal decomposition. *J Fluid Mech*. 2017;828:175-195.
23. Ali N, Hamilton N, DeLucia D, Bayoal R. Assessing spacing impact on coherent features in a wind turbine array boundary layer. *Wind Energy Science (Online)*. 2018;3(1):43-56.
24. Sørensen JN, Mikkelsen RF, Henningson DS, Ivanell S, Sarmast S, Andersen SJ. Simulation of wind turbine wakes using the actuator line technique. *Philos Trans R Soc A Math*. 2015;373(2035):20140071.
25. Bastine D, Vollmer L, Wächter M, Peinke J. Stochastic wake modelling based on pod analysis. *Energies*. 2018;11(3):612.
26. Debnath M, Santoni C, Leonardi S, Iungo GV. Towards reduced order modelling for predicting the dynamics of coherent vorticity structures within wind turbine wakes. *Philos Trans R Soc A Math Phys Eng Sci*. 2017;375:20160108.
27. Iungo GV, Viola F, Camarri S, Porté-Agel F, Gallaire F. Linear stability analysis of wind turbine wakes performed on wind tunnel measurements. *J Fluid Mech*. 2013;737:499-526.
28. Viola F, Iungo GV, Camarri S, Porté-Agel F, Gallaire F. Prediction of the hub vortex instability in a wind turbine wake: stability analysis with eddy-viscosity models calibrated on wind tunnel data. *J Fluid Mech*. 2014;750:R1.
29. Okulov VL, Sørensen JN. Stability of helical tip vortices in a rotor far wake. *J Fluid Mech*. 2007;576:1-25.
30. Kang S, Yang X, Sotiropoulos F. On the onset of wake meandering for an axial flow turbine in a turbulent open channel flow. *J Fluid Mech*. 2014;744: 376-403.

31. Medici D, Alfredsson PH. Measurements on a wind turbine wake: 3D effects and bluff body vortex shedding. *Wind Energy: An Int J Prog Appl Wind Power Convers Technol*. 2006;9(3):219-236.
32. Iungo GV, Wu Y-T, Porté-Agel F. Field measurements of wind turbine wakes with lidars. *J Atmos Ocean Technol*. 2013;30(2):274-287.
33. Aitken ML, Lundquist JK. Utility-scale wind turbine wake characterization using nacelle-based long-range scanning lidar. *J Atmos Ocean Technol*. 2014; 31(7):1529-1539.
34. Santoni C, Carrasquillo K, Arenas-Navarro I, Leonardi S. Effect of tower and nacelle on the flow past a wind turbine. *Wind Energy*. 2017;20:1927-1939.
35. Pierella F, Stran L. Wind tunnel investigation on the effect of the turbine tower on wind turbines wake symmetry. *Wind Energy*. 2017;20(10):1753-1769. https://doi.org/10.1002/we.2120
36. Foti D, Yang X, Guala M, Sotiropoulos F. Wake meandering statistics of a model wind turbine: insights gained by large eddy simulations. *Phys Rev Fluids*. 2016;1(4):044407.
37. Foti D, Yang X, Shen L, Sotiropoulos F. Effect of wind turbine nacelle on turbine wake dynamics in large wind farms. *J Fluid Mech*. 2019;869:1-26.
38. Santoni C, Ciri U, Rotea M, Leonardi S. Development of a high fidelity CFD code for wind farm control. In: 2015 American Control Conference (ACC) IEEE; 2015:1715-1720.
39. De Tullio D, De Palma P, Iaccarino G, Pascazio G, Napolitano M. An immersed boundary method for compressible flows using local grid refinement. *J Comput Phys*. 2007;225(2):2098-2117.
40. Sørensen JN, Shen WZ. Numerical modeling of wind turbine wakes. *J Fluids Eng*. 2002;124(2):393-399.
41. Martínez-Tossas LA, Churchfield MJ, Leonardi S. Large eddy simulations of the flow past wind turbines: actuator line and disk modeling. *Wind Energy*. 2015;18(6):1047-1060.
42. Pope SB, Pope SB, Eccles PJ, Press CU. *Turbulent Flows*. Cambridge: Cambridge University Press; 2000.
43. Ciri U, Salvetti MV, Carrasquillo K, Santoni C, Iungo GV, Leonardi S. Effects of the subgrid-scale modeling in the large-eddy simulations of wind turbines. *Direct and large-eddy simulation x*. Cham: Springer; 2018:109-115.
44. Ciri U, Petrolo G, Salvetti MV, Leonardi S. Large-eddy simulations of two in-line turbines in a wind tunnel with different inflow conditions. *Energies*. 2017;10(6):821.
45. Krogstad P, Eriksen PE. "Blind test" calculations of the performance and wake development for a model wind turbine. *Renew Energy*. 2013;50: 325-333.
46. Bartl JMS, Sætran LR. Blind test comparison of the performance and wake flow between two in-line wind turbines exposed to different turbulent inflow conditions. *Wind Energy Science*. 2017;2:55-76.
47. Sarlak H, Meneveau C, Sørensen JN. Role of subgrid-scale modeling in large eddy simulation of wind turbine wake interactions. *Renew Energy*. 2015; 77:386-399.
48. Orlandi P. *Fluid Flow Phenomena: A Numerical Toolkit*. Vol 55. Springer Science & Business Media; 2012:22–23.
49. Krogstad P, Eriksen PE. Blind test Workshop Calculations for a modell wind turbine; 2011.
50. Orlanski I. A simple boundary condition for unbounded hyperbolic flows. *J Comput Phys*. 1976;21:251-269.
51. Reynolds WC, Hussain AKMF. The mechanics of an organized wave in turbulent shear flow. Part 3. Theoretical models and comparisons with experiments. *J Fluid Mech*. 1972;54(2):263-288.
52. Vermeer LJ, Sørensen JN, Crespo A. Wind turbine wake aerodynamics. *Prog Aerosp Sci*. 2003;39(6-7):467-510.
53. Mo J-O, Choudhry A, Arjomandi M, Lee Y-H. Large eddy simulation of the wind turbine wake characteristics in the numerical wind tunnel model. *J Wind Eng Ind Aerodyn*. 2013;112:11-24.
54. Sørensen JN, Mikkelsen R, Sarmast S, Ivanell S, Henningson D. Determination of wind turbine near-wake length based on stability analysis. In: Journal of physics: Conference series, Vol. 524 IOP Publishing; 2014:012155.
55. Medici D. Experimental studies of wind turbine wakes: power optimisation and meandering. *Ph.D. Thesis*: KTH; 2005.
56. Mao X, Sørensen JN. Far-wake meandering induced by atmospheric eddies in flow past a wind turbine. *J Fluid Mech*. 2018;846:190-209.
57. Gupta V, Wan M. Low-order modelling of wake meandering behind turbines. *J Fluid Mech*. 2019;877:534-560.
58. Lignarolo L, Ragni D, Scarano F, Ferreira CS, Van Bussel G. Tip-vortex instability and turbulent mixing in wind-turbine wakes. *J Fluid Mech*. 2015;781: 467-493.
59. Cal RB, Lebrón J, Castillo L, Kang HS, Meneveau C. Experimental study of the horizontally averaged flow structure in a model wind-turbine array boundary layer. *JRSE*. 2010;2(1):013106.
60. Sørensen JN, Shen WZ. Computation of wind turbine wakes using combined Navier–Stokes/actuator-line methodology. In: 1999 European Wind Energy Conference and Exhibition; 1999:156-159.
61. Churchfield MJ, Schreck S, Martínez-Tossas LA, Meneveau C, Spalart PR. An advanced actuator line method for wind energy applications and beyond. In: 35th Wind Energy Symposium, 2017; 2017:1-20.
62. Orlandi P, Leonardi S. DNS of turbulent channel flows with two-and three-dimensional roughness. *J Turbul*. 2006;7:N73.
63. Iaccarino G, Verzicco R. Immersed boundary technique for turbulent flow simulations. *Appl Mech Eng*. 2003;56(3):331-347.
64. Rocchio B, Ciri U, Salvetti MV, Leonardi S. Appraisal and calibration of the actuator line model for the prediction of turbulent separated wakes. *Wind Energy*. 2020;23(5):1231-1248.
65. Towne A, Schmidt OT, Colonius T. Spectral proper orthogonal decomposition and its relationship to dynamic mode decomposition and resolvent analysis. *J Fluid Mech*. 2018;847:821-867.

How to cite this article: De Cillis G, Cherubini S, Semeraro O, Leonardi S, De Palma P. POD-based analysis of a wind turbine wake under the influence of tower and nacelle. *Wind Energy*. 2020;1–25. https://doi.org/10.1002/we.2592

APPENDIX A

A.1 | Actuator line and immersed boundary methods

Rotor blades are simulated employing the actuator line method (ALM) similar to that proposed by Sørensen and Shen.[60] The ALM models the forces exerted by the blades on the fluid on the basis of the two-dimensional performance of blade's airfoils at each radius, given by the lift, C_L, and drag, C_D, coefficients. Rotor blades are treated as rotating rigid lines, which are divided into discrete segments. For each segment, the relative inflow velocity, u_{rel}, and the angle of attack, α, are evaluated, as shown in Figure A1. Then, knowing the fluid density, ρ, the chord, c, and the twist angle, ϕ, distributions along the blade radius, it is possible to estimate the lift and drag forces per unit length as follows:

$$F_L = \frac{1}{2}\rho u_{rel}^2 C_L(\alpha) c f, \tag{A1}$$

$$F_D = \frac{1}{2}\rho u_{rel}^2 C_D(\alpha) c f. \tag{A2}$$

The coefficient f is a modified Prandtl correction factor,[34] which is meant to account for performance degradation due to tip and root vortices. The calculated aerodynamic forces, F_L and F_D, are spread on areas perpendicular to each actuator line with the following Gaussian distribution kernel:

$$\eta = \frac{1}{\epsilon^2 \pi} \exp\left[-\left(\frac{r_\eta}{\epsilon}\right)^2\right], \tag{A3}$$

where r_η is the radial distance from the actuator line and ϵ is a parameter proportional to the standard deviation of the distribution, which controls forces' spreading. Here, we have taken $\epsilon = 0.025$, which is larger than 2Δ, with $\Delta = \sqrt{\Delta x^2 + \Delta y^2 + \Delta z^2}$, as prescribed by Martinez-Tossas et al.[41] The ALM is an attractive way for simulating rotor blades, because it is computationally less expensive with respect to computing the detailed flow past the blade by a body-fitted grid, especially when dealing with wind farms, where a large number of turbines have to be simulated. However, it must be considered that the ALM presents some limitations; for example, it cannot reproduce some flow features such as the effect of the blade boundary layer separation at high angle of attack. A particular care should be taken in the setting of the velocity sampling used to compute angles and forces, since it can significantly affect the overall performance of the turbine,[61] thus requiring a thorough validation.

The tower and nacelle are described using the immersed boundary method (IBM),[39,62] which avoids the use of a body-fitted grid, reducing the computational cost of the simulations. In particular, a discrete forcing approach, in which the forcing is introduced in the discretized equations, similar to the approach proposed by Orlandi and Leonardi,[62] has been used. This method has been already applied to a large number of flows, as described in the review article by Iaccarino and Verzicco,[63] and validated in the case of wind turbines by Santoni et al.[34] A comment about the particular choice of the IBM and the ALM for modeling the tower and the blade airfoils, respectively, is in order. The IBM, as implemented in the present paper, is very effective in imposing the impermeability condition and in predicting a realistic value of the drag. However, computing accurately the pressure distribution and the position of the separation point over the surface of streamlined bodies at relatively high Reynolds numbers, as in the present case, requires a high-resolution mesh with the size of the cell much smaller than the chord length. Since the tip of the blade

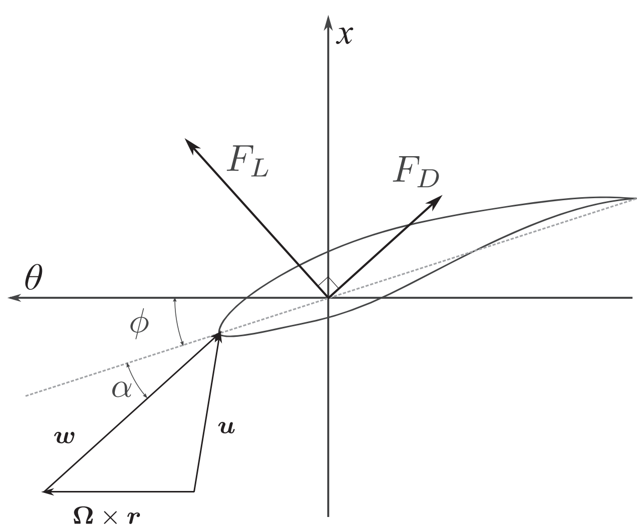

FIGURE A1 Blade cross section: θ and x indicate the tangential and axial directions, respectively, and $\boldsymbol{\Omega} \times \boldsymbol{r}, \boldsymbol{u}, \boldsymbol{w}$ represent the projection in the blade-to-blade plane of the blade speed and of the absolute and relative flow velocity, respectively has a chord length $c \approx 0.03D$, it is unfeasible to resolve in a three-dimensional computation the details of the flow using the IBM. Instead, using the ALM, one describes the interaction between the airfoil and the fluid by assigning a lift force (viz., a circulation), which is obtained from lookup tables constructed by accurate simulations of the 2D steady flow around the airfoil. Due to the high mesh resolution one can achieve at the blade tip using a 2D airfoil model, the lift force employed in the ALM is more accurate than that obtained by an "underresolved" IBM. On the other hand, the IBM is quite accurate when modeling the tower because its diameter is larger, $d_t/D = 0.1$, and it is possible to have a sufficient number of points inside the body to enforce impermeability and to provide an accurate evaluation of the drag. In fact, the present IBM allows one to impose null velocity at each point inside the body. Instead, using the ALM, a forcing term is added to the Navier–Stokes equations, which represents the time-averaged overall force experienced by the body. Such a forcing term is spread (with a Gaussian shape) on a cylindrical region of the mesh which may not resemble the pressure distribution of the "real body." As a consequence, at a generic point, the distributed force of the ALM may not balance the momentum of the incoming flow and the impermeability condition at the body surface cannot be satisfied accurately, as shown in Rocchio et al.[64] Moreover, the ALM applied to the tower would provide a steady symmetric wake. Attempts have been made to impose a force varying in time to provide an oscillation of the tower wake (see Sarlak et al.[47]). This approach would, however, require assuming a priori the shedding frequency, which instead is not needed for the IBM. For these reasons, the approach used in the present paper combines the two methods. When the dimensions of the solid body are sufficiently larger than the mesh size (6–8 times in each direction), we use the IBM because it is more accurate than the ALM. Otherwise, when the dimensions of the body are too small to be treated with the IBM, the ALM is used to impose the average overall effect of the body on the fluid.

A.2 | Proper orthogonal decomposition

Turbulent flows are often characterized by the presence of coherent spatiotemporal structures. The proper orthogonal decomposition (POD) is a statistically based method for extracting these organized structures from time-dependent experimental or numerical (direct numerical simulation [DNS] and large eddy simulation [LES]) data.

The method is based on finding a deterministic function $\boldsymbol{\phi}(\boldsymbol{z})$ that is, on average, *an optimal approximation* of a stochastic variable $\boldsymbol{q}(\boldsymbol{z},\xi)$, where $\boldsymbol{z}$ is a set of independent variables and ξ is a point in the sample space.[10]

The space-only variant of the POD[65] applied to fluid flows described by space–time fields $\boldsymbol{q}(\boldsymbol{x},t)$ considers the flow at each instant as a realization of a stochastic process. Therefore, the basic objective of the method is formalized by finding the spatial mode $\boldsymbol{\phi}(\boldsymbol{x})$ that maximizes the quantity:

$$\lambda = \frac{E\{|\langle \boldsymbol{q}(\mathbf{x},t), \boldsymbol{\phi}(\mathbf{x})\rangle|^2\}}{\langle \boldsymbol{\phi}(\mathbf{x}), \boldsymbol{\phi}(\mathbf{x})\rangle}, \tag{A4}$$

assuming that the stochastic process belongs to a Hilbert space,$\mathcal{H}$, with inner product $\langle \cdot , \cdot \rangle$ and $E\{\cdot\}$ is the expectation operator. In the case of space-only POD, the expectation operator corresponds to a time average and the inner product is defined as

$$\langle \boldsymbol{u}, \boldsymbol{v}\rangle = \int_\Omega \mathbf{v}^*(\mathbf{x},t)\boldsymbol{W}(\mathbf{x})\boldsymbol{u}(\mathbf{x},t)d\mathbf{x}, \tag{A5}$$

where $\boldsymbol{u}$ and $\boldsymbol{v}$ are two elements in$\mathcal{H}$, Ω is the spatial flow domain, $\boldsymbol{W}(\boldsymbol{x})$ is a positive-definite Hermitian weight tensor, and the asterisk superscript indicates the Hermitian transpose. The maximization problem in Equation (A4) can be reformulated, using a standard variational method, such as the Fredholm eigenvalue problem:

$$\int_\Omega \mathbf{C}(\mathbf{x},\mathbf{x}')\boldsymbol{W}(\mathbf{x}')\boldsymbol{\phi}(\mathbf{x}')d\mathbf{x}' = \lambda\boldsymbol{\phi}(\mathbf{x}), \tag{A6}$$

where $\mathbf{C}(\mathbf{x},\mathbf{x}') = E\{\boldsymbol{q}(\mathbf{x},t)\boldsymbol{q}^*(\mathbf{x}',t)\}$ is the two-point spatial correlation tensor. The latter is a compact, self-adjoint, positive operator and $\int_\Omega \mathbf{C}(\mathbf{x},\mathbf{x})d\mathbf{x} < \infty$, and, as such, it carries some properties that characterize the eigenvalue problem (A6):

- Hilbert–Schmidt theory guarantees that there exists a countably infinite set of eigenpairs $\{\lambda_j, \boldsymbol{\phi}_j\}$.
- All the eigenvalues λ_j are real and nonnegative so that they can be ordered as $\lambda_1 \geq \lambda_2 \geq \cdots \geq 0$.. The largest eigenvalue λ_1 of Equation (A6) with its associated eigenfunction $\boldsymbol{\phi}_1(\mathbf{x})$ constitute the mode that maximizes Equation (A4).
- The eigenfunctions are orthonormal, $\langle \boldsymbol{\phi}_j, \boldsymbol{\phi}_k\rangle = \delta_{jk}$, providing a complete basis for each realization of the stochastic process $\boldsymbol{q}(\mathbf{x},t)$.

Consequently, as reported in Equation (7), the unsteady flow field can be expanded as a sum of these orthonormal eigenfunctions, appropriately weighted by the time coefficients $a_j(t)$ which can be shown to be uncorrelated at zero time lag:

$$E\{a_j(t)a_k(t)\} = \lambda_j \delta_{jk}. \tag{A7}$$

In most cases, when considering either experimental or numerical dataset, one deals with discretized flow fields, both in space and time. In order to perform the space-only POD of these data, a sufficiently large number (M) of instantaneous snapshots of the flow field is required. Usually, the three velocity components (u_1,u_2,u_3) are considered so that each snapshot can be stored as a N vector $\boldsymbol{q}^i$, where $N = 3\times S$ and S is, in turn, the number of grid points. One can build then a matrix $\mathbf{Q}\in\mathbb{R}^{N\times M}$ representing all dataset, in which each column is a single snapshot,

$$\mathbf{Q} = \begin{bmatrix} | & | & | & & | \\ \mathbf{q}^1 & \mathbf{q}^2 & \mathbf{q}^3 & \dots & \mathbf{q}^M \\ | & | & | & & | \end{bmatrix}. \tag{A8}$$

The two-point correlation tensor can be then approximated by the matrix $\mathbf{C}\in\mathbb{R}^{N\times N}$ according to the following equations:

$$\mathbf{C} = \frac{1}{M}\mathbf{Q}\mathbf{Q}^T, \tag{A9}$$

$$\mathbf{C}_{ij} = \frac{1}{M}\sum_{k=1}^{M} \mathrm{q}_i^k \mathrm{q}_j^k \approx E\{q_i q_j\}. \tag{A10}$$

The Fredholm eigenvalue problem (A6) is therefore approximated by the following eigenvalue problem:

$$\mathbf{CW\Phi} = \mathbf{\Phi\Lambda}, \tag{A11}$$

$$\mathbf{\Phi}^T\mathbf{W\Phi} = \mathbf{I}, \tag{A12}$$

where the positive-definite symmetric (Hermitian) matrix $\mathbf{W}\in\mathbb{R}^{N\times N}$ accounts for both the weight $\boldsymbol{W}(\mathbf{x})$ and the numerical quadrature on a discrete grid, the columns of $\mathbf{\Phi}$ represent the eigenvectors, that is, the POD modes, whereas the diagonal entries of $\mathbf{\Lambda}$ are the eigenvalues λ_j.

There are two main alternatives to solve the discrete counterpart of the eigenvalue problem in Equation (A6): (i) computing the singular value decomposition (SVD) of the snapshot matrix **Q** and (ii) using the so-called "snapshot POD"[11], based on the solution of a smaller eigenvalue problem. In the present work, the first method is employed, and since the grid used for the discretization of the data is uniform, the weight matrix is considered unitary. Therefore, the POD is performed by computing the SVD of the snapshot matrix **Q**, divided by the square root of the number of snapshots M,

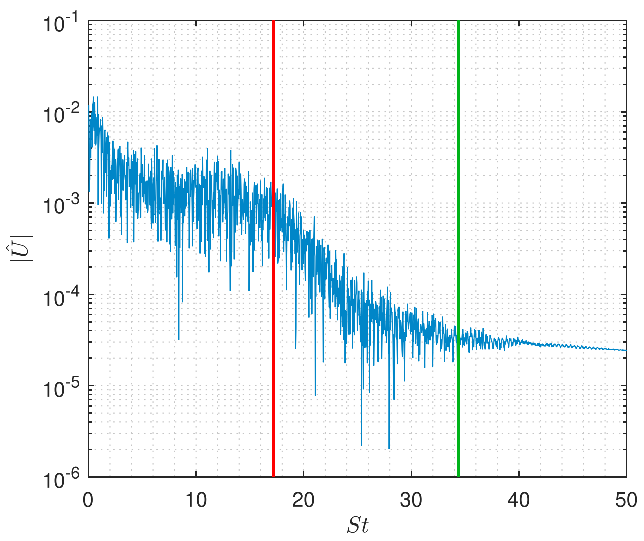

FIGURE A2 Amplitude spectrum of the streamwise velocity signal $U(t)$ from a probe located on the rotor axis at six diameters past the wind turbine. The green and red line represent the sampling frequency of the proper orthogonal decomposition snapshots and the related Nyquist frequency, respectively [Colour figure can be viewed at wileyonlinelibrary.com]

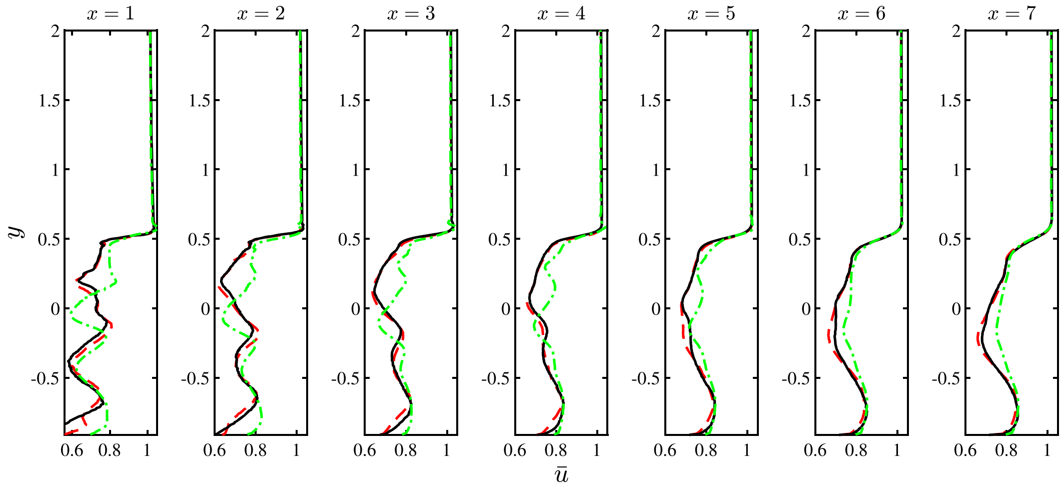

FIGURE A3 Time-averaged streamwise velocity profiles at 7 locations along the midline of the computational domain for three different computational grids: the coarsest grid (– · – · –) consists of $1000 \times 250 \times 250$ gridpoints in x, y and z directions, respectively; the intermediate grid (– – – –) consists of $1600 \times 400 \times 400$ gridpoints; the finest grid (———) consists of $2048 \times 512 \times 512$ gridpoints [Colour figure can be viewed at wileyonlinelibrary.com]

$$\frac{\mathbf{Q}}{\sqrt{M}} = \mathbf{USV}^T, \tag{A13}$$

where the left singular vectors $\mathbf{U}$ correspond to the right eigenvectors of $\mathbf{C}$, namely, to the POD modes, and $\mathbf{S}$ is the matrix of the singular values, such that $\mathbf{SS}^T = \mathbf{\Lambda}$. The time coefficients of each POD mode, a_k, are given by the rows of the matrix $\sqrt{M}\mathbf{SV}^T$. The method has been implemented using tools from the LAPACK libraries and convergence of the POD modes has been assessed considering several dataset made by an increasing number of snapshots.

Moreover, we have opportunely chosen the frequency threshold for data sampling for it to be sufficiently higher than the frequency of the coherent structures populating the flow. Figure A2 shows the Fourier amplitude spectrum of the streamwise velocity signal extracted from a probe located on the rotor axis, at six diameters past the turbine. The green and the red lines represent the sampling frequency of the POD snapshots and the related Nyquist frequency, respectively. The Nyquist frequency, being equal to 17.19, is quite high with respect to the recovered flow structures, since it corresponds to the frequency of the sixth harmonic of the tip vortices. Moreover, one can observe that the amplitude decreases exponentially after the red line, meaning that energy-containing structures are those with lower frequencies. Therefore, we believe that further increasing the sampling rate would not change the energy-containing coherent structures we presented in the results.

A.3 | Mesh convergence

The convergence of the numerical results with respect to the mesh has been assessed with respect to several time-averaged velocity profiles: Figure A3 shows the streamwise velocity distributions along the y direction, at seven locations ($x = \{1,2,3,4,5,6,7\}$) along the midline of the computational domain. Three different computational grids have been employed with $1000 \times 250 \times 250$, $1600 \times 400 \times 400$, and $2048 \times 512 \times 512$ gridpoints in x, y, and z directions, respectively. The solutions obtained using the two finest grids, being very close to each other, indicate that grid convergence is achieved.

According to the Kolmogorov's hypotheses, the Kolmogorov length scale $\eta \equiv \left(\nu^3/\epsilon\right)^{1/4}$, for the present case, is equal to $4.64 \cdot 10^{-5}$ (in rotor diameter units), where the dissipation rate ϵ has been estimated as U_∞^3/D. Therefore, the resulting size of the finest mesh, being approximately equal to 0.006 in each direction, is approximately 130 times the Kolmogorov length scale and, according to existing literature on turbulent flows, lies in the inertial subrange.[42] Moreover, the fine mesh size is similar to that employed in previous computations and validations using the same numerical approach for solving problems involving wind turbine flows.[26,34]